AGU PUBLICATIONS

JGR

Journal of Geophysical Research: Solid Earth

RESEARCH ARTICLE

10.1002/2016JB013120

Estimates of aseismic slip associated with small earthquakes near San Juan Bautista, CA

J. C. Hawthorne[1], **M. Simons**[2], **and J.-P. Ampuero**[2]

[1]School of Earth and Environment, University of Leeds, Leeds, UK, [2]Seismological Laboratory, Division of Geological and Planetary Sciences, California Institute of Technology, Pasadena, California, USA

Key Points:
- Observe postseismic strain of small (mostly M<4) earthquakes near San Juan Bautista, CA
- The 1.5 day postseismic moment is comparable to coseismic moment
- Observed postseismic to coseismic moment ratio is independent of magnitude

Supporting Information:
- Supporting Information S1
- Supporting Information S2
- Table S1
- Table S2

Correspondence to:
J. C. Hawthorne,
J.C.Hawthorne@leeds.ac.uk

Citation:
Hawthorne, J. C., M. Simons, and J.-P. Ampuero (2016), Estimates of aseismic slip associated with small earthquakes near San Juan Bautista, CA, *J. Geophys. Res. Solid Earth*, *121*, 8254–8275, doi:10.1002/2016JB013120.

Received 25 APR 2016
Accepted 8 OCT 2016
Accepted article online 12 OCT 2016
Published online 9 NOV 2016

Abstract Postseismic slip observed after large ($M > 6$) earthquakes typically has an equivalent moment of a few tens of percent of the coseismic moment. Some observations of the recurrence intervals of repeating earthquakes suggest that postseismic slip following small ($M \lesssim 4$) earthquakes could be much larger—up to 10 or 100 times the coseismic moment. We use borehole strain data from U.S. Geological Survey strainmeter SJT to analyze deformation in the days before and after 1000 $1.9 < M < 5$ earthquakes near San Juan Bautista, CA. We find that on average, postseismic strain is roughly equal in magnitude to coseismic strain for the magnitude range considered, suggesting that postseismic moment following these small earthquakes is roughly equal to coseismic moment. This postseismic to coseismic moment ratio is larger than typically observed in earthquakes that rupture through the seismogenic zone but is much smaller than was hypothesized from modeling repeating earthquakes. Our results are consistent with a simple, self-similar model of earthquakes.

1. Introduction

Afterslip observed following large earthquakes typically releases a moment comparable to a few tens of percent of the coseismic moment [e.g., *Donnellan and Lyzenga*, 1998; *Segall et al.*, 2000; *Gahalaut et al.*, 2008; *Johanson and Bürgmann*, 2010; *Cetin et al.*, 2012; *D'Agostino et al.*, 2012; *Lin et al.*, 2013; *Gonzalez-Ortega et al.*, 2014]. The afterslip moment varies from event to event, from a few percent of coseismic [*Paul et al.*, 2007; *Dogan et al.*, 2014] to more than 100% [e.g., *Bürgmann et al.*, 2001; *Langbein et al.*, 2006; *Freed*, 2007]. However, the postseismic to coseismic moment ratios observed for large ($M \gtrsim 6$) earthquakes do not vary strongly with earthquake magnitude (see *Lin et al.* [2013], *Fattahi et al.* [2015], and Figure 10 for summaries). Such a magnitude-independent ratio suggests that earthquakes may be self-similar—that earthquakes of different sizes are scaled versions of the same processes.

However, it has been suggested that the self-similar scaling breaks for very small earthquakes. Investigations of small repeating earthquakes reveal recurrence intervals that are surprisingly long given the estimated seismic slip [*Nadeau and Johnson*, 1998; *Chen et al.*, 2007]. *Chen and Lapusta* [2009] proposed that these long recurrence intervals result in part from large postseismic slip. Their model predicts that small ($M < 3$) repeating earthquakes should have postseismic moments that are 10 to 100 times larger than their seismic moments.

In this study, we estimate coseismic and postseismic moments for M 1.9–5 earthquakes near San Juan Bautista, CA. We use data from U.S. Geological Survey (USGS) borehole strainmeter SJT, which has recorded more than 1000 $M \geq 1.9$ earthquakes since 1983. We introduce the data in section 3. In section 4, we consider the individual records of several M 3–5 earthquakes. The records of most smaller earthquakes have low signal-to-noise ratios, so in section 5 we develop a method to stack the strain from about 1000 events. We present the stacked strain signals in section 6, and in section 7 we discuss their implications for repeating and nonrepeating earthquakes.

2. Motivation: Recurrence Intervals of Repeating Earthquakes

Repeating earthquakes are earthquakes that are inferred to periodically rupture the same patch of a given fault. If the earthquakes release all of the slip that accumulates on the patch, the cumulative seismic slip must match the long-term slip rate. The slip per earthquake should equal the product of the background slip rate and the recurrence interval.

Slip in an earthquake can also be estimated directly from the observed seismic moment if a rupture model and stress drop are assumed [e.g., *Madariaga*, 1976; *Aki and Richards*, 2002]. Observed stress drops are typically between 0.1 and 100 MPa and show little dependence on magnitude [e.g., *Abercrombie*, 1995; *Prieto et al.*, 2004; *Imanishi and Ellsworth*, 2006; *Allmann and Shearer*, 2007]. *Nadeau and Johnson* [1998] and *Nadeau et al.* [2004] therefore compared the moment-derived slip assuming a magnitude-independent 3 MPa stress drop with the slip expected from the recurrence intervals of repeating earthquakes on the creeping section of the San Andreas Fault (SAF). For a M 4 earthquake, the moment-derived slip was about 4 times smaller than the recurrence interval-derived slip. For a M 2 earthquake, the moment-derived slip was more than 10 times smaller.

The increased difference for the M 2 earthquakes illustrates that not only are the recurrence intervals longer than expected, they scale differently from the predictions [*Nadeau and Johnson*, 1998; *Nadeau et al.*, 2004; *Chen et al.*, 2007]. Conventional earthquake models predict that slip should scale with the cube root of the moment, as $M_0^{1/3}$, if stress drop is magnitude independent [e.g., *Madariaga*, 1976; *Aki and Richards*, 2002]. However, slips derived from recurrence intervals scale roughly as $M_0^{0.17}$ [*Nadeau and Johnson*, 1998; *Nadeau et al.*, 2004; *Chen et al.*, 2007].

To explain the discrepancy in the estimated slips, *Nadeau and Johnson* [1998] proposed that stress drops in repeating earthquakes vary with magnitude, unlike stress drops in nonrepeating earthquakes. However, observations near Parkfield, CA, including many repeating earthquakes have not revealed magnitude-dependent stress drops [*Imanishi et al.*, 2004; *Imanishi and Ellsworth*, 2006; *Allmann and Shearer*, 2007; *Abercrombie*, 2014]. As alternative explanations, *Dreger et al.* [2007] suggested the high stress drops were confined to small areas within the larger rupture. *Anooshehpoor and Brune* [2001] proposed that the recurrence intervals of repeating earthquakes vary with proximity to locked regions, and *Sammis and Rice* [2001] proposed that some of the slip in each repeating earthquake patch is released in larger earthquakes that rupture through it. Finally, *Beeler et al.* [2001] proposed that "extra" slip occurs aseismically. In the model of *Beeler et al.* [2001], significant aseismic slip was distributed throughout the interseismic period, and aseismic slip rates were higher later in the interseismic interval. Similar aseismic slip was also seen between moderately sized earthquakes in the rate and state model of *Chen and Lapusta* [2009], with aseismic moment up to 5 times the coseismic moment distributed throughout the interseismic period. But for the smallest earthquakes in their models, the aseismic slip budget was dominated by slip that occurred just after the earthquakes. This postseismic slip could accumulate moment up to 100 times the coseismic moment. The large postseismic slip coupled with more distributed interseismic slip allowed the earthquakes modeled by *Chen and Lapusta* [2009] to have recurrence intervals that scaled like the observed recurrence intervals.

In this study, we look for evidence for the hypothesized large postseismic slip in the 1.5 days following M 1.9 – 5 earthquakes near San Juan Bautista, CA. We estimate the ratio of postseismic to coseismic moment as a function of earthquake magnitude for repeating and nonrepeating earthquakes.

3. Strain Records

In order to estimate the postseismic moment, we use data from the borehole strainmeter SJT, which is located at the northern end of the creeping section of the SAF, about 1.5 km southwest of the surface trace (Figure 1). SJT was installed in 1983 for the USGS [*Gladwin et al.*, 1987]. In the last few decades several thousand earthquakes with $M > 1$ have occurred within 10 km of the station and are identified in the Northern California Seismic Network (NCSN) catalog. Many of these events have been relocated by *Waldhauser* [2009] and define a plane that strikes N135°E and dips 80° to the SW (Figure 2).

The strain data have an 18 min sampling interval. They have been cleaned, processed, and calibrated by J. Langbein and others at the USGS. In addition, we identify and remove times with probable instrumental errors or nontectonic noise. The problematic times are listed in the supporting information. We also estimate and remove three recurring nontectonic signals: a 3 h instrumental signal, tides, and a response to atmospheric pressure. This processing is further described in Text S2.

Figure 3 shows the strain records of several earthquakes after removing nontectonic signals. The record in Figure 3a clearly illustrates the coseismic and postseismic signals of two earthquakes: a M 3.7 and a M 4.2. The coseismic signal of a M 3.6 earthquake is visible in Figure 3b. This smaller earthquake's postseismic signal is

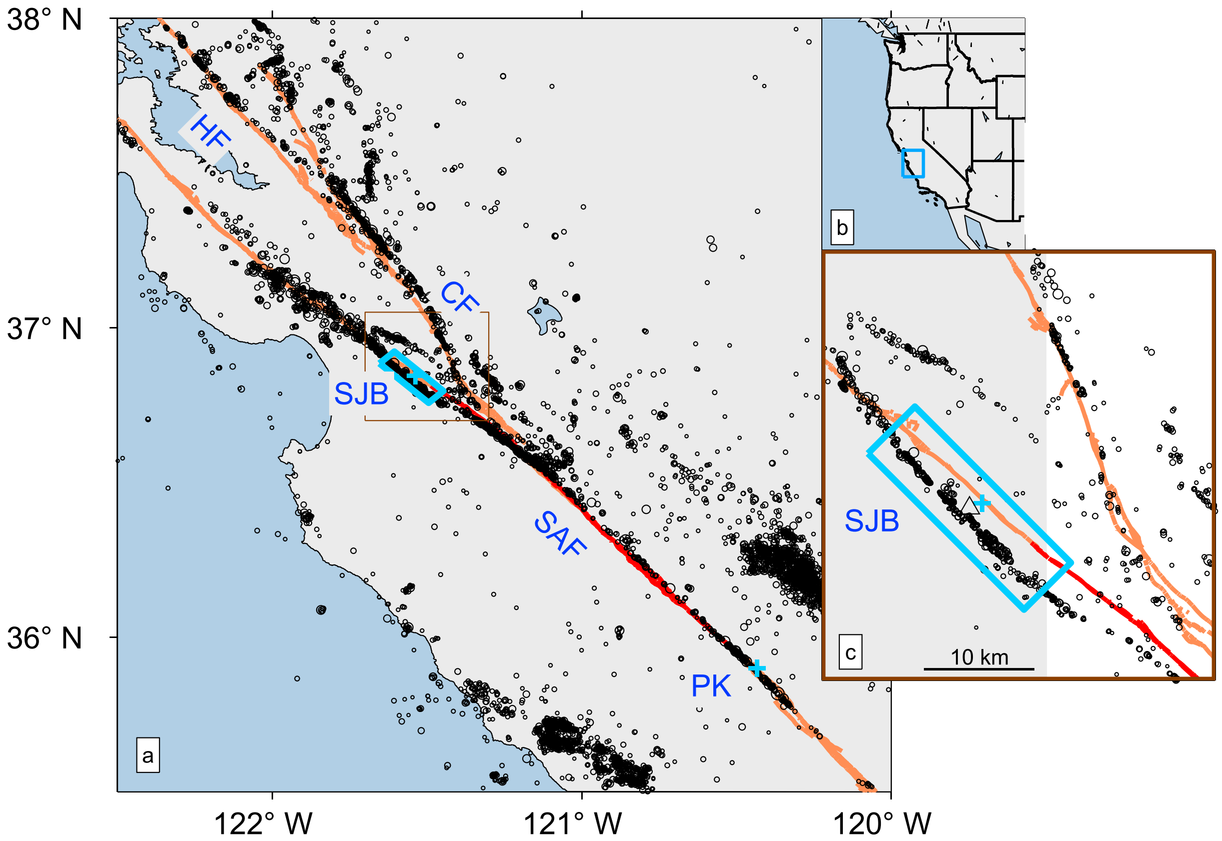

Figure 1. Illustration of the study area. (a) The regional context, (b) Larger context, with the region of interest marked with the blue box. (c) An expanded view of the area within the brown box in Figure 1a. We use data from earthquakes located in the blue box near San Juan Bautista (SJB), marked with a blue cross in Figures 1a and 1c. San Juan Bautista is located near the northern end of the creeping section of the SAF (dark red lines), which extends south to Parkfield (PK), marked with another blue cross. Orange lines indicate other sections of the San Andreas (SAF), Calaveras (CF), and Hayward Faults (HF). Fault traces are taken from the USGS and California GS quaternary fault database. Black circles indicate $M > 2.5$ earthquakes from the NCSN catalog, with relocations from *Waldhauser* [2009] where available. The black triangle in Figure 1c indicates the location of the strainmeter.

less clear, however, and the strain from a *M* 3.1 earthquake that occurred a few hours earlier is not resolvable above the noise.

The observed postseismic strain could come from two sources: afterslip and poroelastic relaxation. Significant viscoelastic deformation is likely to occur only at much longer timescales than the 2 days we will consider here, assuming material properties are similar to those inferred for larger earthquakes [e.g., *Pollitz et al.*, 2006; *Johnson et al.*, 2009; *Bruhat et al.*, 2011]. We interpret our results in terms of afterslip. We cannot rule out large poroelastic strain, but we consider it less likely. In section 7.3 and Text S11, we consider several non-earthquake signals observed at the strainmeter that suggest that there is little poroelastic deformation at SJT. Nevertheless, we note that any poroelastic shear strains would likely have the same sign as strain produced by afterslip (see section 7.3). Since we interpret the postseismic strain as afterslip, we would map any poroelastic strain into additional afterslip and overestimate the afterslip moment.

Assuming that afterslip is the dominant signal in the strain records, the observations can be easily interpreted. The earthquakes considered here are small. Their spatial extents are at most a few percent of their distance from the strainmeter. From the perspective of the recorded strain, the coseismic and postseismic slip occur in the same place. Changes in strain are therefore proportional to moment, and each strain time series can be thought of as a time history of moment.

The moment accumulation is reflected in all three components of horizontal strain. Figure 3 illustrates these components: areal ($\epsilon_{E+N} = \epsilon_{EE} + \epsilon_{NN}$, in red), differential extension ($\epsilon_{E-N} = \epsilon_{EE} - \epsilon_{NN}$, in yellow), and engineering shear ($2\epsilon_{EN}$, abbreviated henceforth as ϵ_{2EN}, in blue). We focus on the differential extension strain (ϵ_{E-N}), which measures simple shear on vertical NE striking or NW striking planes. Slip on the NW striking SAF

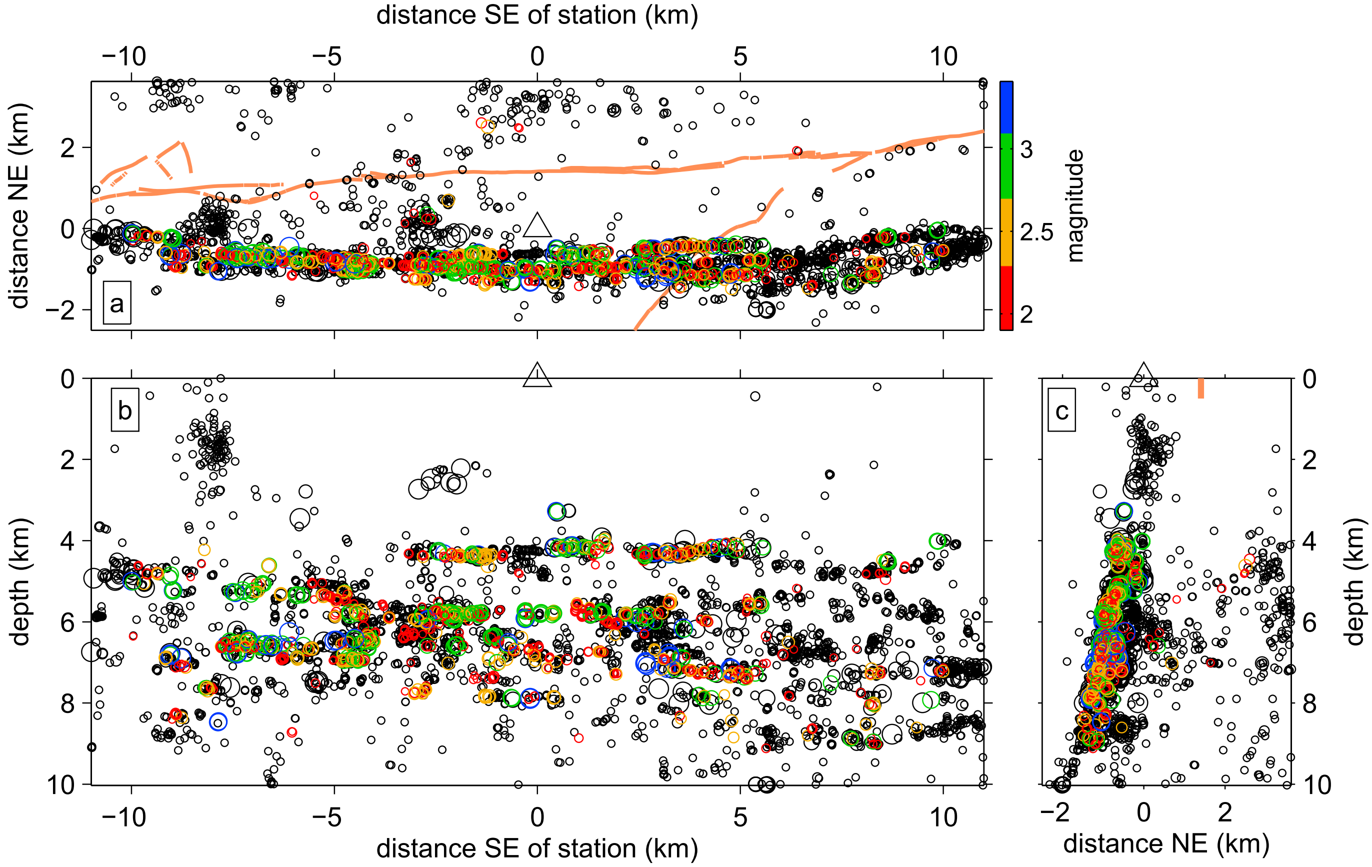

Figure 2. Illustration of the local seismicity and earthquakes considered. Circles indicate earthquakes in the NCSN catalog. Most have been relocated by *Waldhauser* [2009]. (a) Map view, oriented along strike. The station is located at the center of the plot (open triangle). Earthquakes used in our inversion are plotted in color, where color indicates magnitude. Earthquakes that are not used are plotted in black. Orange lines mark the surface trace of the SAF as recorded in the USGS and California GS quaternary fault database. (b) Depth view of seismicity, looking from the SW. (c) Depth view of seismicity, looking from the SE.

produces a spatial pattern of ϵ_{E-N} strain with maxima near strainmeter SJT (see Figure S1b). The ϵ_{E-N} Green's function varies slowly with location near the station, so predictions of the coseismic ϵ_{E-N} are relatively robust. In contrast, it is difficult to correctly predict the coseismic ϵ_{E+N} and ϵ_{2EN} at SJT, as the Green's functions for these components have nodal planes near the strainmeter (Figure S1a and S1c).

Throughout this paper, when we predict coseismic strains, we assume that the earthquakes consist of horizontal slip on a fault in an elastic half space with shear modulus 30 MPa and Poisson's ratio 0.25 [*Okada*, 1985]. The fault strikes N135°E and dips 80°SW. However, our conclusions are relatively insensitive to the details of the coseismic strain prediction.

4. Estimates of Postseismic Moment in Large Events

4.1. Observed Offsets

The coseismic and postseismic strain are well resolved for 19 earthquakes recorded at SJT. Plots of their strain time series are shown in Figures S5–S23. For each earthquake, we estimate two strain offsets. The "coseismic" offset is the change in strain between 20 min before the earthquake and 20 min after it. The "total" offset is the change in strain between 20 min before the earthquake and 1.5 days after it. A 1.5 day postseismic interval is chosen as representative of the total strain because strain is poorly resolved at longer timescales. We discuss the implications of the chosen timing in sections 6.2 and 7.

The coseismic and total strain offsets are plotted against earthquake magnitude in Figure 4a, where the offsets have been normalized by the predicted coseismic strain. Figure 4b shows the strain ratios: the total offsets divided by the observed coseismic offsets. Each component of strain is considered separately, and the different components are distinguished by color. Yellow is used for ϵ_{E-N}, the best-resolved strain component.

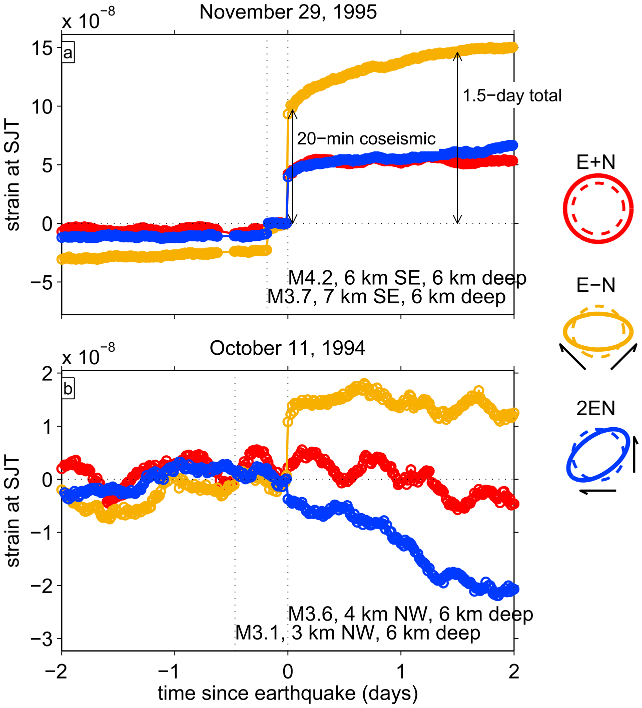

Figure 3. Strain records of a few earthquakes near San Juan Bautista. (a) Two well-recorded earthquakes: a *M* 3.7 followed a few hours later by a *M* 4.2. Both the coseismic and postseismic strain are resolvable for the *M* 4.2. Color indicates the three components of strain. We focus on the differential extension component (E-N, yellow), as it is largest and most robust for modeling. (b) Earthquakes with smaller strain signals: a *M* 3.1 followed a few hours later by a *M* 3.6. The coseismic strain from the *M* 3.6 is clear, but the postseismic strain is not above the noise. Strain from the *M* 3.1 is well below the noise.

The error bars in Figure 4 are 90% confidence intervals on the strain offsets. To estimate these uncertainties, we extract 3000 20 min and 1.5 day offsets from data intervals without earthquakes. We add these noise offset pairs to each earthquake offset pair to obtain probability distributions for the earthquake offsets. We plot the earthquake offsets in Figure 4 only if the 90% confidence interval on the ratio of total to coseismic strain is smaller than 4.

Figure 4b shows that the ratio of the total to coseismic strain is usually between 1.5 and 2.5. This ratio shows little to no dependence on magnitude. On the other hand, Figure 4a suggests that the ratio of the observed offsets to the predicted coseismic strain is larger for smaller earthquakes. This magnitude dependence is at least partly a selection bias. Smaller earthquakes with strains close to the predicted strains are not visible above the noise. For $M > 3.5$ earthquakes recorded on the best-resolved component, ε_{E-N}, the prediction-normalized offsets do not vary systematically with magnitude.

4.2. Discrepancy in the Predicted and Observed Coseismic Strains

We must note, however, that the observed coseismic offsets differ from the predictions, even for many of the larger earthquakes. The observed ε_{E-N} offsets exceed the predictions by a factor of 2 to 10, and the ε_{E+N} and ε_{2EN} offsets sometimes even have a different sign than the predictions. These sign errors can plausibly be explained by just 10° uncertainty in the fault orientation (see Figure S2), as the strainmeter is close to the nodal plane for these components. The systematically large ε_{E-N} offsets are more puzzling. In section 6 we will find similarly large coseismic offsets—3 to 5 times the predictions—for stacks of smaller earthquakes.

We discuss several possible explanations for the larger-than-expected coseismic offsets in Text S3. Several tens of percent error in the predictions could result from a number of uncertainties, including errors in the assumed fault orientation, uncertainties in the strainmeter calibration [*Langbein*, 2010, 2015], unmodeled vertical stratification in the elastic moduli [*Cattin et al.*, 1999; *Segall*, 2010] (section 5.5.3), or systematic errors in the earthquake depths. To explain the factor of 3 error with earthquake location uncertainties, most of the earthquakes would have to be factor of 1.5 shallower than we have assumed. Larger errors—perhaps a factor

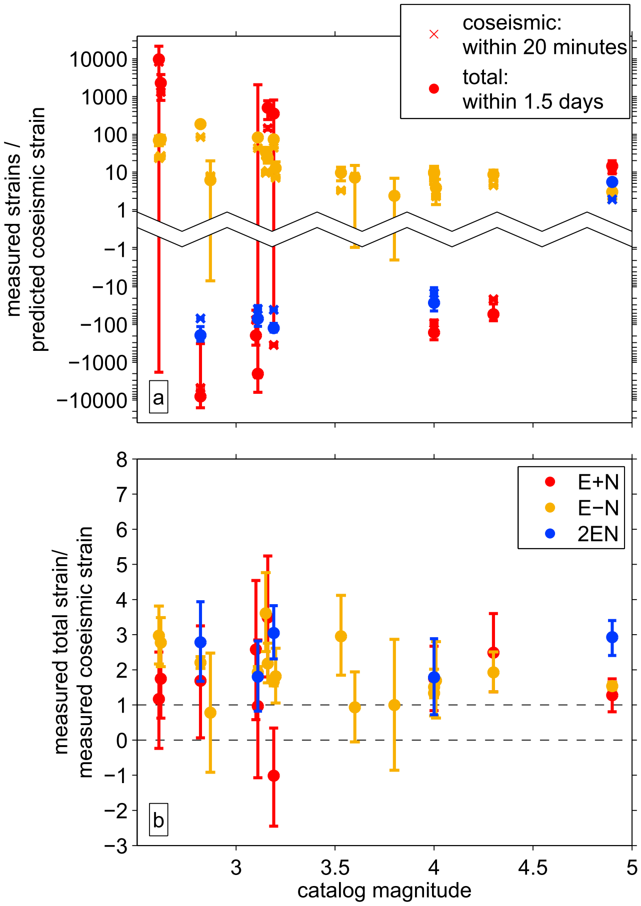

Figure 4. (a) Estimated strain offsets divided by the strain predicted from the seismic moment. Crosses show the coseismic strain change: from 20 min before the earthquakes to 20 min after. Circles show the total strain change: from 20 min before to 1.5 days after. Color indicates the component. Estimated offsets with the same sign as the prediction plot as positive numbers, above the scale break. Offsets with the opposite sign plot as negative numbers, below the scale break. Error bars delimit 90% confidence intervals. Error bars that cross the break in scale indicate that the 90% uncertainty allows for strains with both signs. (b) Total (1.5 day) strain offset divided by the coseismic (20 min) strain offset. In both panels, offsets are plotted only if the 90% confidence interval on the total to coseismic ratio is less than 4.

of 2—could arise if the elastic moduli vary horizontally, perhaps because of fault zone or cross-fault structure, as is sometimes suggested by larger-scale seismic and geodetic observations [*Eberhart-Phillips and Michael*, 1993; *Chen and Freymueller*, 2002; *Schmalzle et al.*, 2006; *Jolivet et al.*, 2009; *Lin et al.*, 2010].

Unmodeled elastic structure could also contribute to systematic errors in seismic moment estimates and thus to a discrepancy in the observed and predicted strain offsets. In addition, there is significant nonsystematic error in the assumed seismic moments. We use the local magnitude recalibration of *Hawthorne et al.* [2016], which provides an accurate local scaling of the relative moments of two earthquakes, but the calibration has up to 50% uncertainty in the absolute scaling—in the average moment of all events.

Finally, we note that the larger-than-expected coseismic ε_{E-N} strain could be a real signal, due to large postseismic slip in the first 20 min. However, by stacking the data from many small earthquakes, we are able to probe the average moment accumulation through time (see section 6.2 and Text S8). The observed decay in moment rate suggests small postseismic moment in the first few minutes.

Given the apparent difficulty in matching the observed offsets, in Text S3 we also consider the possibility that the offsets are not the static elastic response to slip at depth but a more complex response to shaking near the borehole. Such a response was suggested by a correlation between static offsets and dynamic velocities at strainmeters in Southern California [*Barbour et al.*, 2015]. With the coseismic offsets observed at SJT, we cannot exclude an important dynamic effect, as there is scatter in the data, and there are a range of possible models for the dynamic response. However, the magnitude and distance scalings of the observed offsets are best matched by the expected static strain scaling, not by one of the dynamic scalings (Figures S3 and S4). As the signs of the observed strains are also consistent with the static predictions within error, we continue to interpret the strain data in the simplest way: as an elastic response to slip at depth.

Assuming discrepancies in the observed and predicted coseismic strains are due to errors in the elastic modeling—either for the strain Green's functions or the seismic moments—we can reduce the uncertainty by focusing on the ratio of the observed strain offsets: the total (1.5 day) offsets divided by the coseismic offsets. As long as postseismic slip occurs on part of the fault close to that of the seismic slip, errors in the elastic structure and seismic moment should change the 20 min and 1.5 day offsets by the same factor and have a negligible effect on the offset ratio.

5. Method for Stacking Strain From Small Earthquakes

We want to examine how the postseismic strain varies with earthquake magnitude. However, most nearby earthquakes with $M < 3.5$ generate coseismic and postseismic strains below the noise level of individual recordings. We therefore stack their signals to obtain average strain histories for groups of earthquakes. The chosen groups include earthquakes with $1.9 \leq M < 2.3$, $2.3 \leq M < 2.7$, $2.7 \leq M < 3.1$, and $3.1 \leq M < 3.5$, though our results are not sensitive to the details of the bin choice.

Not all earthquakes can be usefully included in the stacks of strain history. Some earthquakes occur at times of instrumental problems or close in time to $M > 3.5$ earthquakes, which are not modeled. Using the selection criteria described in Text S5, we retain 1098 of the approximately 1500 $M \geq 1.9$ earthquakes within 10 km of strainmeter SJT. Of these events, 518 are $1.9 \leq M < 2.3$, 287 are $2.3 \leq M < 2.7$, 229 are $2.7 \leq M < 3.1$, and 64 are $3.1 \leq M < 3.5$.

5.1. Forward Model for Earthquake Strain

For each group of earthquakes, we extract a normalized strain history, or a normalized moment history. We model the observed strain as the sum of these normalized moment histories, scaled by the relevant seismic moment and Green's function. For instance, the strain due to a single earthquake k is modeled as

$$\varepsilon(t) = \underbrace{M_{0k}}_{\text{seismic moment}} \quad \underbrace{G(x_k)}_{\text{Green's function}} \quad \underbrace{f_{m(k)}(t - t_k)}_{\text{normalized strain history}} \quad . \tag{1}$$

Here $f_m(t')$ is the normalized moment history for magnitude group m. t' is modeled time since the earthquake, t is the time of the observed strain, and the earthquake occurs at time t_k and location x_k. The Green's functions $G(x_k)$ are calculated for horizontal strike slip on a SW dipping fault in a half space, as described in section 3 [*Okada*, 1985].

When multiple earthquakes occur in succession, the observed strain $\mathrm{d}(t)$ records their combined signal, as illustrated in Figure 5. We model the observed strain $\mathrm{d}(t)$ as a sum over earthquakes k:

$$\mathrm{d}(t) = \sum_k M_{0k} G(x_k) f_{m(k)}(t - t_k) + \text{noise}. \tag{2}$$

From Figure 5 and equation (2), we can see how the strain observed at time t depends on the normalized strains f_m at time t'. We thus rewrite equation (2) in matrix form as

$$\mathbf{d} = \mathbf{G}_e \mathbf{f} + \text{noise}. \tag{3}$$

Here $\mathbf{d}_i = \mathrm{d}(t_i)$. $\mathbf{f}$ is the set of normalized strain time series f_m, and $\mathbf{G}_e$ accounts for the moments, Green's functions, and time shifts.

Each time series $f_m(t')$ is parameterized as a piecewise linear function with 103 nodes between $t' = -1$ and $t' = 2$ days. The time spacing varies linearly from 10 minutes just after the earthquakes to 4 h 2 days afterward. There is a 6 min interval centered on the earthquake times.

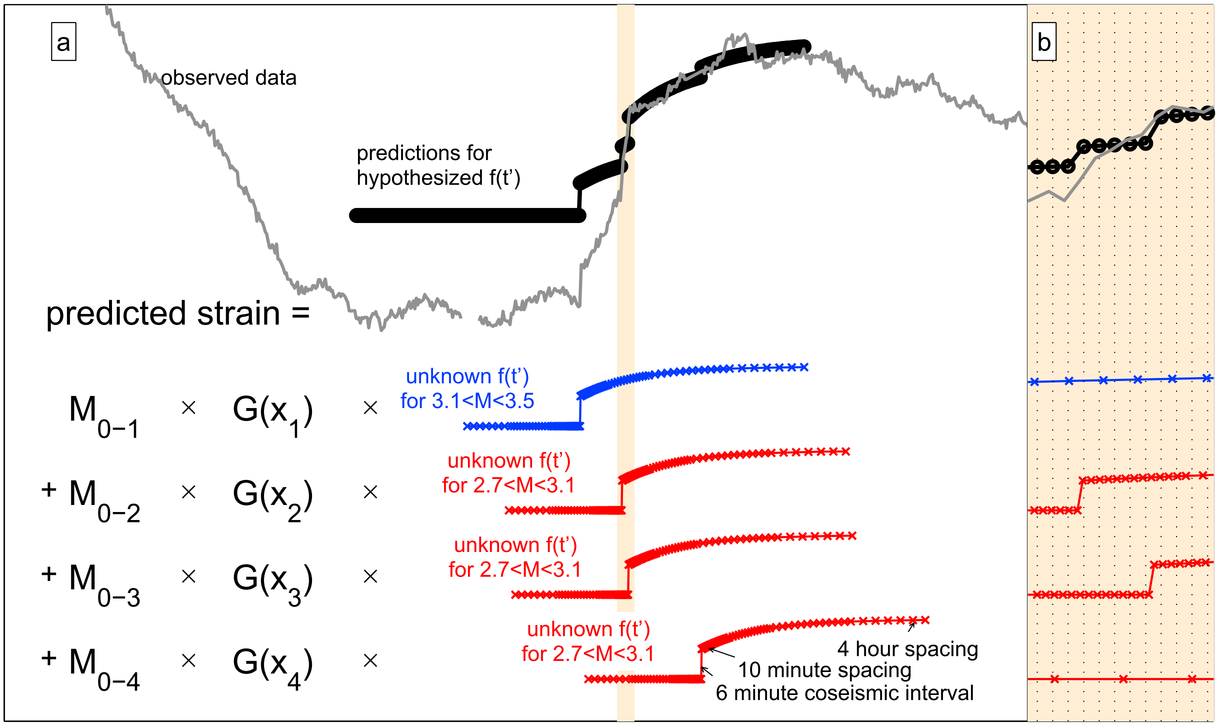

Figure 5. (a) Illustration of the model to extract average normalized strain histories $f(t')$ (red and blue) for groups of earthquakes. The observed data (gray) is modeled with the normalized strain histories (red and blue) of the relevant earthquakes, scaled by their moments M_{0-k} and Green's functions $G(x_k)$. (b) The predicted strain for the hypothesized strain histories shown is plotted in black. As is typical, the predictions account for only a fraction of the observed strain (gray), as much variation in the observed strain is noise. Figure 5b shows an enlargement of the beige interval in Figure 5a to illustrate the sampling of the data and the modeled time series.

5.2. Filtering and Noise Model

In our analysis, we model only 1.5 days of postseismic strain because the signal is poorly resolved at longer timescales. To avoid modeling long-period noise, we high-pass filter the data and the forward model with a corner period of 10 days, using a two-pole Butterworth filter. In the context of equation (3), this filtering can be viewed as a linear operator F. The model becomes

$$\mathbf{Fd} = \mathbf{FG}_e\mathbf{f} + N(\mathbf{C}). \tag{4}$$

Noise is assumed to follow a multivariate Gaussian distribution with temporal covariance matrix **C**. The temporal covariance **C** accounts for the tendency of closely spaced observations to experience similar noise [e.g., *Langbein and Johnson*, 1997; *Hawthorne and Rubin*, 2013]. We construct **C** from the data in Text S6. We can now solve for the normalized strain time series $f_m(t')$, which remain unfiltered.

Equation (4) includes several large matrices, with 30 years of data sampled every 18 min. To solve for the normalized strain time series more quickly, we divide the 30 year strain record into overlapping 20 day segments. As described in Text S7, we simultaneously fit data from all segments but do not allow temporal covariance in the noise between segments.

6. Results

The solid lines in Figure 6 show the best fitting strain time series obtained from our inversions. They are shifted vertically so that the average strain is zero in the 1–3 h before the earthquakes. Each strain time series shows a step at the time of the earthquakes, followed by further accumulation in the subsequent hours to days. The best fitting coseismic (20 min before and after) strain accumulations are 3 to 5 times the strain predicted from the seismic moments. The best fitting total (20 min before to 1.5 days after) strain accumulations are 7 to 11 times the predicted coseismic step. As discussed in section 4.2 and Text S3, the larger-than-expected coseismic offsets are most likely due to errors in the Green's functions or in the absolute seismic moment calibration. To reduce the uncertainty, we will focus on the ratio of the total to the coseismic strain offsets.

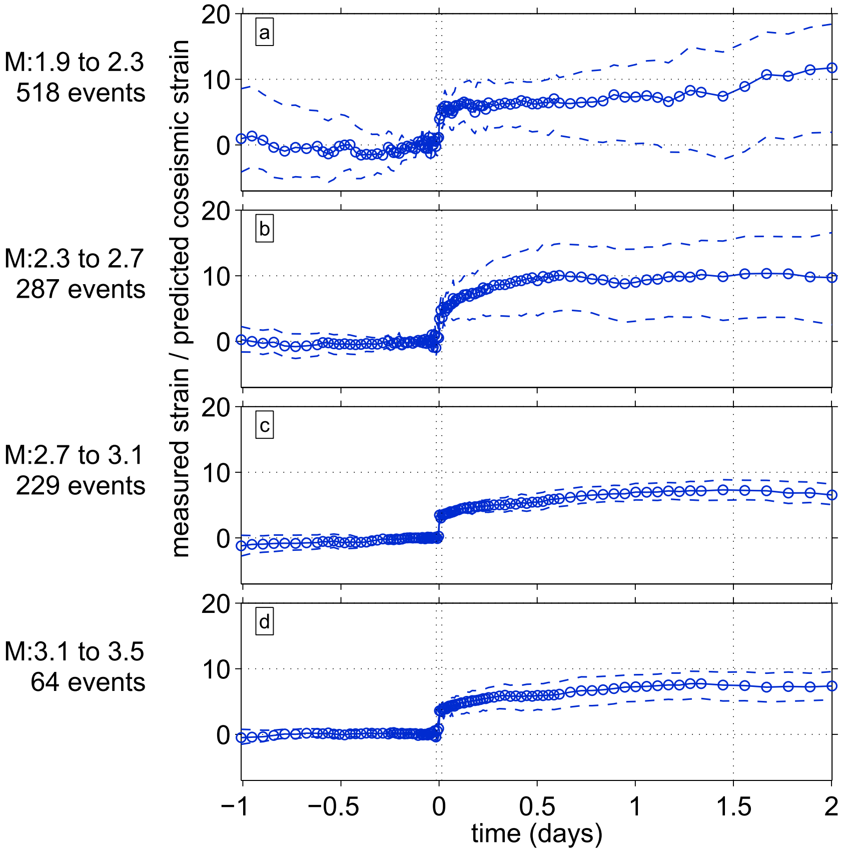

Figure 6. Estimated normalized strain time series, shifted vertically so that the average strain is zero in the 3 h before the earthquakes. For all magnitude groups, the coseismic strain is between 3 and 6 times the prediction, and the strain accumulated within 1.5 days of the earthquake is between 7 and 11 times the predicted coseismic. The dashed blue lines include 90% of the values obtained from bootstrapping. Vertical dotted lines delimit the defined coseismic period, 20 min before and after the earthquakes, and the postseismic period, within 1.5 days.

The strain offsets and their ratios are plotted as a function of magnitude in Figure 7. The best fitting total-to-coseismic ratios are between 1.5 and 2.5 for all magnitude groups. For comparison with these moment estimates, the dashed line in Figure 7a illustrates the total strain expected if postseismic slip accommodates the long recurrence intervals of small repeating earthquakes (see section 2). In plotting the expected strain, we have assumed that the coseismic and total ruptures have the same stress drops, so that the moments predicted by the recurrence intervals scale with the predicted slips cubed. With this assumption, the moment ratios predicted from the recurrence intervals are clearly larger than those we infer from the data. The discrepancy between the prediction and data would increase further if we assumed that the total rupture had a smaller stress drop than the coseismic event, as the lower stress drop would require a larger moment to match the same recurrence interval-derived slip. The discrepancy could be reduced if we assumed that the total rupture had a larger stress drop than the coseismic rupture, but that assumption seems unphysical, as it is the coseismic stress drop that is thought to be the primary driver of transient slip.

6.1. Error Estimates

The error bars in Figures 6 and 7 are 90% confidence intervals from bootstrapping. To obtain them, we divide the strain data into 25 time intervals. The intervals are chosen such that each one includes roughly the same number of earthquakes. For each bootstrap sample, we pick 25 out of the 25 intervals, with replacement, and invert for a strain time series. Histograms of bootstrapped offsets are shown Figure S24a, S24e, and S24i. The dashed lines in Figure 6 enclose 90% of the strain values obtained, and the bars in Figure 7 enclose 90% of the extracted offsets. In Text S9 in the supporting information we consider an alternative approach to estimating errors and invert parts of the data that do not have earthquakes. The uncertainties are similar to those obtained via bootstrapping.

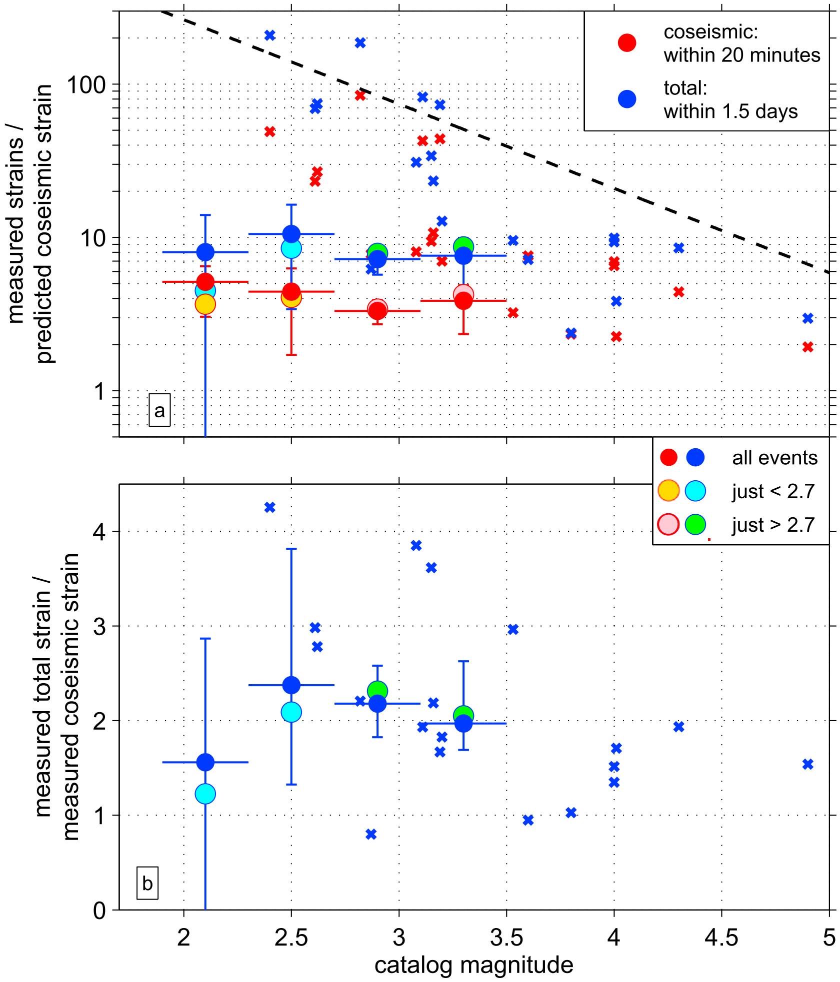

Figure 7. (a) Estimated strain offsets relative to the predicted seismic step. Red is for the coseismic step (20 min before the earthquakes to 20 min after), and blue is for the total step (20 min before to 1.5 days after). (b) Estimated total (1.5 day) strain steps as a function of magnitude, normalized by the estimated coseismic strain. In both panels, the blue and red circles with error bars are the values obtained for small earthquakes in section 5, and the small crosses are estimates for the individual large events from section 4. The yellow and cyan circles indicate the coseismic and total offsets obtained by considering only earthquakes smaller than *M* 2.7. The pink and green circles indicate the coseismic and total offsets obtained by considering only earthquakes larger than *M* 2.7. In all cases, both the coseismic and total steps are roughly constant with magnitude. The dashed black line is the ratio of total to coseismic strain that would be expected if postseismic slip explained the entire observed scaling of the recurrence intervals of repeating earthquakes (see section 2). The dashed line is missing from Figure 7b because the expected values would plot above the plot limits.

6.2. Accumulation With Time

The estimated uncertainties in strain accumulation are small enough that we can also consider shorter time intervals. The blue circles and bars in Figure 8 shows offsets and confidence intervals for four postseismic intervals: 5–20 min, 20 min–1.3 h, 1.3–5.3 h, and 5.3–21.3 h. These four intervals have equal lengths in log time; time since the earthquakes increases by a factor of 4 in each one. Afterslip moment rate after large earthquakes is often observed to decay with time as t^{-1}, so that intervals with equal log time have equal amounts of postseismic moment [e.g., *Marone et al.*, 1991; *Perfettini and Avouac*, 2004; *Hsu et al.*, 2006; *Savage and Langbein*, 2008]. This logarithmic accumulation can reasonably match the strain accumulation for the *M* 1.9–2.7 earthquakes in Figures 8a and 8b, which have relatively large uncertainties. The red crosses in Figure 8 indicate a constant accumulation per $\log(t)$ interval, chosen to be 0.28 to match the data.

For the better-resolved *M* 2.7–3.5 earthquakes in Figures 8c and 8d, the strain accumulation appears to increase from the first interval to the last. This increase suggests that the strain rate decreases more slowly than t^{-1}. For instance, a t^{-1} decay would predict that the strain rate would decrease by a factor of 16 from

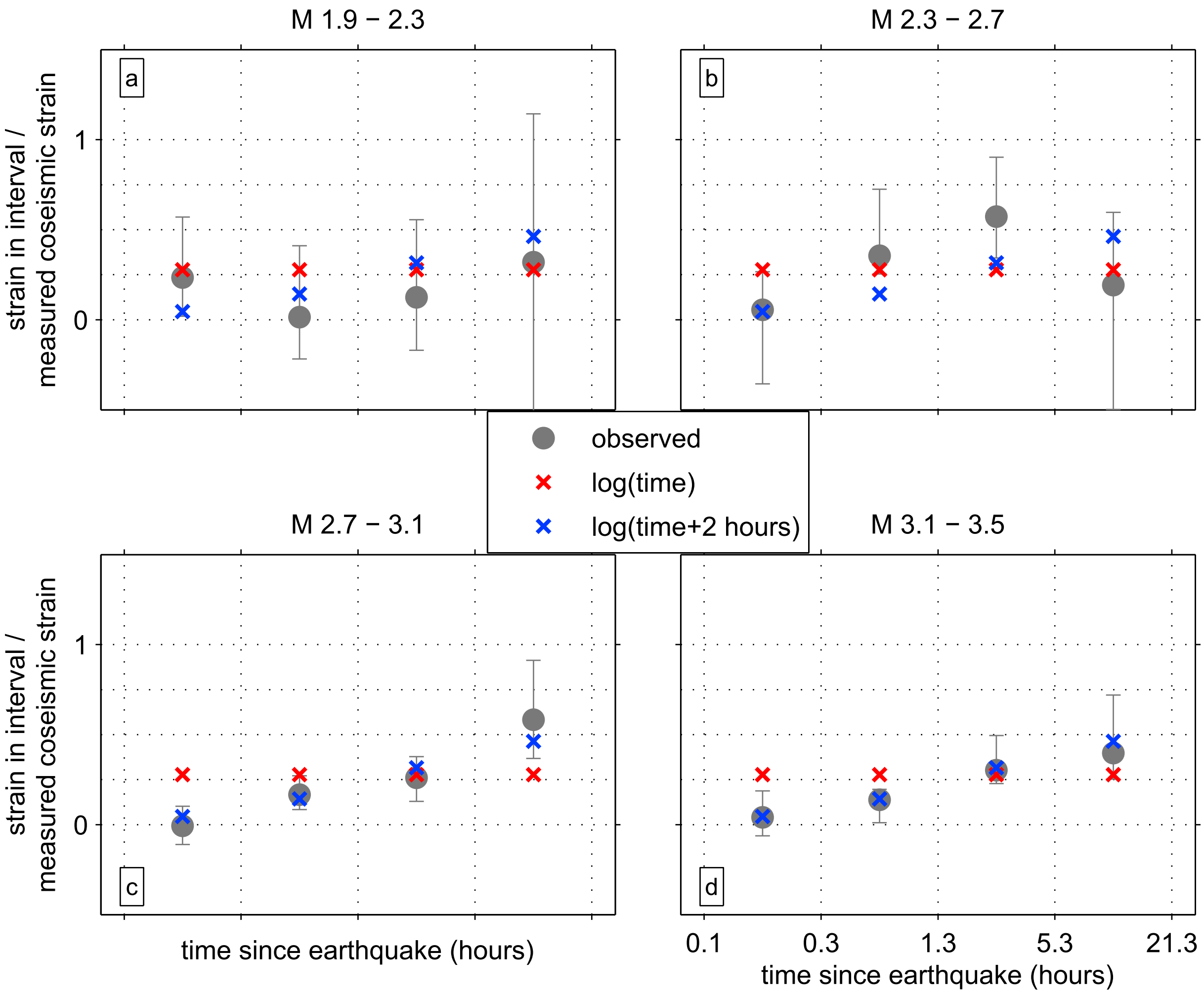

Figure 8. Observed evolution of postseismic strain in the hours following the earthquakes, as compared with strain that accumulates as log(time + t_c), where t_c is a cutoff time. The gray circles with error bars show strain offsets and 90% confidence intervals in four postseismic time ranges: 5–20 min, 20–80 min, 80 min–5.3 h, and 5.3–21.3 h. (a and b) For the two smallest magnitude bins, the strain in each time range is roughly the same or at least shows no pattern with time. The red crosses show a constant value in each bin, as would be expected if moment accumulates as log(time). The chosen value of 0.28 was picked to match the data. (c and d) For the two large magnitude bins, the strain per interval increases with time. The blue crosses indicate the pattern of offsets expected if strain accumulates as log(time + 2h). See text for details.

the second interval to the fourth, but the best fitting strain offsets increase by a factor of 3 between these intervals, suggesting that the strain rate decreased only by a factor of $16/3 \approx 5$.

The slow early decay may indicate an initiation timescale for postseismic slip. An initiation period is present in models of velocity-strengthening friction and appears in the moment accumulation equations as a cutoff time t_c, so that moment accumulates as $\log(t+t_c)$ [e.g., *Marone et al.*, 1991; *Montési*, 2004; *Perfettini and Avouac*, 2004; *Savage*, 2007]. The strain offsets for the M 2.7–3.5 stacks are well matched by cutoff times between 0.5 and 5 h. The blue crosses in Figure 8 show the predicted strain for a cutoff of time of 2 h.

6.3. Results for Repeating Earthquakes

One motivation of this study is to look for large postseismic slip that could explain the long recurrence intervals of repeating earthquakes [*Chen and Lapusta*, 2009], and we do not see that slip in Figure 7. However, most of the earthquakes considered here are not repeaters. *Taira et al.* [2014] estimate that just 20% of the earthquakes in the 30 km south of strainmeter SJT are repeating earthquakes. Forty-nine of the 1000 earthquakes used in our stacks were identified as repeaters by *Templeton et al.* [2008]. They examined seismicity between 1984 and 2005 in a region that includes the southern half of the earthquakes considered here. It is possible that repeating earthquakes are somehow different from “normal” earthquakes. For instance, one might imagine that the frictional parameters in regions of repeating earthquakes mean that repeaters are closer in size to the

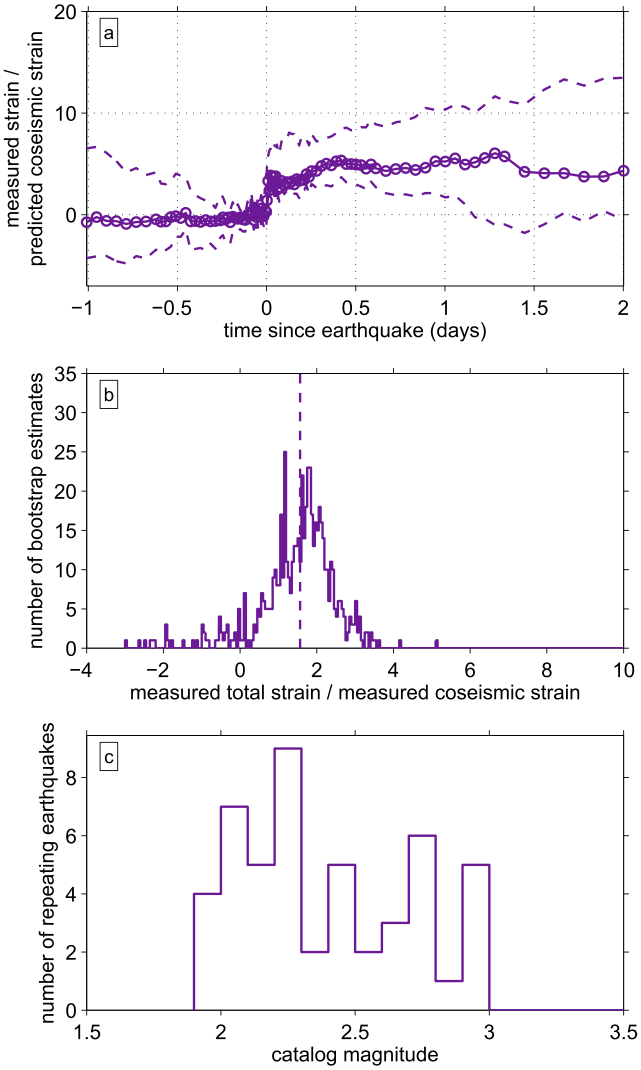

Figure 9. Average strain time series and offsets estimated for the 49 repeating earthquakes identified by *Templeton et al.* [2008], when these events are separated into their own group. (a) Strain time series for the repeating earthquake group. As in Figure 6, the curves are shifted so that the average strain is zero in the 3 h before the earthquakes. The dashed lines include 90% of the values obtained from bootstrapping. (b) Distribution of bootstrapped ratios of the 1.5 day strain to the 20 min strain. The vertical dashed line is the best fitting value. The values suggest moderate postseismic slip, less than 2 times the coseismic moment. (c) Histogram of the magnitudes of the 49 repeating earthquakes used in the stack.

minimum earthquake size dictated by friction. As such, repeaters may be more likely than most earthquakes to behave like the small earthquakes in the model of *Chen and Lapusta* [2009] and thus to have larger postseismic slip than most earthquakes.

In order to investigate the postseismic moment of repeating earthquakes specifically, we isolate the 49 earthquakes identified as repeaters by *Templeton et al.* [2008]. We remove these earthquakes from their magnitude groups and place them in their own group. We now solve for a strain time series for each of five bins: four magnitude bins and one repeating earthquake bin. The strain time series obtained for the four original magnitude groups are insignificantly different from those in Figure 6.

The strain time series for the repeating earthquake group is shown in Figure 9a. Figure 9b shows a histogram of the bootstrapped ratios of the total to coseismic offsets. The strain for this group is noisier since only 49 earthquakes are included, but the estimated strains are similar to those estimated in the other groups. Ninety percent confidence intervals place the ratio of the total to coseismic strain between 0 and 3, not > 10 as would be required to match the recurrence intervals of $M < 3$ earthquakes [e.g., *Nadeau and Johnson*, 1998; *Nadeau et al.*, 2004; *Chen et al.*, 2007].

6.4. Addressing Possible Sources of Bias in the Estimated Strain

The results and error estimates we have obtained constrain the ratio of postseismic to coseismic moment to be nearly constant with magnitude. However, there are aspects of our analysis that our bootstrap error estimates may neglect. In this section and the supporting information, we address several possible biases.

6.4.1. Mapping Strain Between Earthquakes

A first potential bias comes from mapping strain between earthquakes. For instance, since small earthquakes often occur near large ones, postseismic strain from large earthquakes could be accommodated in our models as extra strain in small earthquakes. However, we do not see a significant trade-off between the strain in different magnitude groups in the bootstrapped estimates. To further address this issue, we redo our analysis with only $M < 2.7$ earthquakes or only $M \geq 2.7$ earthquakes. The estimated values are plotted along with the results from the entire catalog in Figure 7. They fall within the range of our error estimates.

A second bias could come from unmodeled earthquakes, as their unmodeled strain could be mapped into the postseismic slip of included events. In Text S5 we identified portions of the data that were particularly vulnerable to such mapping and excluded them. We also redo our analysis two more times, once without these exclusions and once with a stricter criterion: requiring that the total strain in excluded earthquakes be less than one fourth the strain in any magnitude bin (see Text S5). Both sets of results fall within the error bars in Figure 7, suggesting that little strain is mapped between earthquake groups.

6.4.2. Variation in Locations and Focal Mechanisms

It is more difficult to assess the effect of incorrectly predicted coseismic strain. If small earthquakes occur in a systematically different location than large events, we might systematically mismodel their Green's functions and overestimate or underestimate their moment. We do not observe any magnitude-dependent locations that would suggest a problem, but we cannot account for small-scale Earth structure.

The strain from small earthquakes could also be incorrectly estimated if small earthquakes have systematically different focal mechanisms. For example, they could occur on more variable fault planes. We have limited information about the fault planes of $M < 3$ earthquakes.

The best way to alleviate these problems is to consider the ratio of the observed postseismic and coseismic strains. Both the postseismic and coseismic strains could be biased, but if they are biased by the Green's functions, they should be biased by the same factor, and the ratio of the two observed strains should experience a smaller error. With this in mind, we focus our interpretation on the estimated strain ratios.

7. Discussion

7.1. A Simple Scaling

We have shown that for about 1000 $M < 4$ earthquakes near San Juan Bautista, the average postseismic moment accumulated within 1.5 days is 50 to 150% of the coseismic moment, independent of the earthquake magnitude. This magnitude-independent ratio is consistent with simple models of earthquake scaling, where earthquakes of different sizes are simply scaled versions of each other.

Our postseismic to coseismic moment ratios can be compared with the postseismic moments of several nearby earthquakes. The 2004 M 6 Parkfield earthquake exhibited about 3 times as much postseismic moment as coseismic moment [*Langbein et al.*, 2006; *Freed*, 2007; *Barbot et al.*, 2009], the 2007 M 5.4 Alum Rock earthquake exhibited 2 times as much [*Murray-Moraleda and Simpson*, 2009], and the 1998 M 5.1 San Juan Bautista earthquake, just south of our study area, exhibited roughly 1.5 times as much postseismic as coseismic moment [*Taira et al.*, 2014]. Two of these postseismic moment ratios are larger than those observed here, but they were estimated over years, not 1.5 days. If we assume that afterslip following the small earthquakes analyzed here continues at a rate proportional to time^{-1} for rate for 4 months, a time period more than 10% of the several year recurrence intervals [e.g., *Nadeau and Johnson*, 1998; *Nadeau et al.*, 2004; *Templeton et al.*, 2008], we would predict postseismic to coseismic moment ratios of 2 to 3, comparable to the ratios observed for the 1998 San Juan Bautista, 2004 Parkfield, and 2007 Alum Rock earthquakes [*Langbein et al.*, 2006; *Freed*, 2007; *Barbot et al.*, 2009; *Murray-Moraleda and Simpson*, 2009; *Taira et al.*, 2014].

On the other hand, the postseismic to coseismic moment ratios observed in this study are significantly larger than those observed for many $M > 6$ earthquakes, which typically display postseismic moments only a few

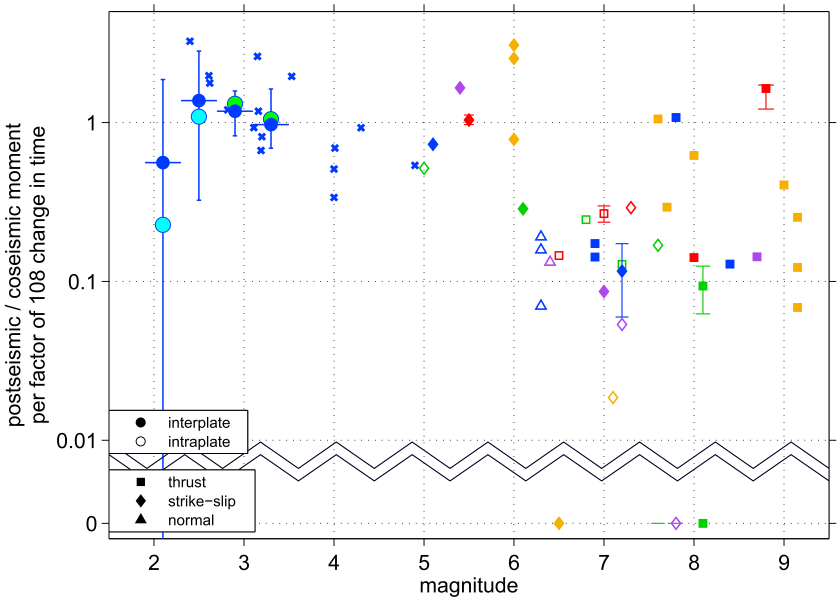

Figure 10. Postseismic slip obtained here along with estimates from larger earthquakes. Moments estimated for $M < 5$ earthquakes are the postseismic moments observed from 20 min to 1.5 days after the earthquakes, relative to the coseismic moments. As in Figure 7, circles are for stacked groups, and crosses are for individual earthquakes. Squares, diamonds, and triangles plotted for larger earthquakes show the estimated postseismic to coseismic moment ratios estimated by *Savage and Svarc* [1997], *Segall et al.* [2000], *Bürgmann et al.* [2001], *Jacobs et al.* [2002], *Melbourne et al.* [2002], *Miura et al.* [2004], *Hsu et al.* [2006], *Langbein et al.* [2006], *Pritchard and Simons* [2006], *Subarya et al.* [2006], *Chlieh et al.* [2007], *Freed* [2007], *Podgorski et al.* [2007], *Ryder et al.* [2007], *Barbot et al.* [2008], *Furuya and Satyabala* [2008], *Jónsson* [2008], *Mahsas et al.* [2008], *Amoruso and Crescentini* [2009], *Murray-Moraleda and Simpson* [2009], *Cheloni et al.* [2010], *Johanson and Bürgmann* [2010], *Ryder et al.* [2010], *Bell et al.* [2012], *Cetin et al.* [2012], *D'Agostino et al.* [2012], *Wen et al.* [2012], *Lin et al.* [2013], *Dogan et al.* [2014], *Gonzalez-Ortega et al.* [2014], *Taira et al.* [2014], *Fattahi et al.* [2015], and *Floyd et al.* [2016].

tens of percent of the coseismic moment [e.g., *Donnellan and Lyzenga*, 1998; *Segall et al.*, 2000; *Hsu et al.*, 2006; *Gahalaut et al.*, 2008; *Johanson and Bürgmann*, 2010; *Cetin et al.*, 2012; *D'Agostino et al.*, 2012; *Lin et al.*, 2013; *Gonzalez-Ortega et al.*, 2014]. In Figures 10 and S27, we plot some of the published postseismic moment ratios for comparison with those obtained here. The moment ratios in Figure 10 are normalized by the logarithm of the observation time interval to simplify the comparison, as postseismic moment often accumulates logarithmically with time after the earthquake [e.g., *Marone et al.*, 1991; *Perfettini and Avouac*, 2004; *Hsu et al.*, 2006; *Savage and Langbein*, 2008]. Here we have normalized to a factor of 108 increase in time to match our 20 min to 1.5 day strain observation interval. For most of the $M > 6$ earthquakes, the time-normalized postseismic moments are less than 25% of the coseismic moment, a factor of 4 smaller than the time-normalized moment ratios for the M 1.9–3.5 earthquakes in this study.

It is difficult to ascertain whether the time normalization is appropriate, as postseismic slip and aftershocks might last longer for larger earthquakes [e.g., *Dieterich*, 1994; *Perfettini and Avouac*, 2004; *Ziv*, 2006]. However, even if we assume that afterslip stops after 1.5 days for small earthquakes but persists from 20 min to 50 years after large events, the postseismic moments following large earthquakes would increase by only a factor of 3, to within a factor of 2 of the postseismic moment ratios estimated for the small earthquakes, but still smaller.

The smaller afterslip of large earthquakes could result in part from their elongate geometry. Large earthquakes are constrained along dip by the seismogenic zone but extend long distances along strike. In Figure 11 we show the postseismic to coseismic moment ratio for two geometries. To mimic small earthquakes, for the red curves we assume a circular coseismic rupture with uniform slip δ_{co} within a radius R. The postseismic slip occupies a ring around the rupture with width aR and average slip δ_{post} equal to δ_{co} or $0.5\delta_{co}$. The postseismic moments are comparable to our observations—between 0.5 and 1.5 times the coseismic moment—when the slip $\delta_{post} = \delta_{co}$, and the ring width aR is between 0.2 and 0.6 times the radius R.

To model larger earthquakes (blue curves), we assume that the coseismic rupture occupies a rectangle with along-dip width W and that postseismic slip occurs in two rectangles updip and downdip of the rupture,

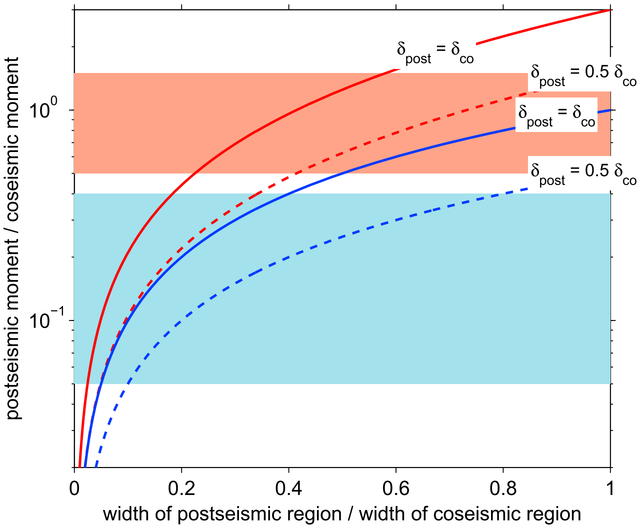

Figure 11. Ratio of postseismic to coseismic moment expected for various geometries. Red lines indicate the ratio for circular ruptures, and blue lines indicate the ratio for elongate ruptures. The x axis shows a, the width of the postseismic region divided by the width of the coseismic zone. For the circular ruptures, the radius of the postseismic region is $(1 + a)$ times the radius of the coseismic region. The average slip in the postseismic area δ_{post} is either half of or equal to the average slip in the coseismic area δ_{co}, as shown by the labels. The shaded regions show the postseismic to coseismic moment ratios observed here (red) and the ratios typically observed in studies of larger earthquakes (blue).

each with along-dip width $aW/2$. Afterslip occurring at the along-strike ends is neglected. In this elongate geometry, when $0.2 < a < 0.6$ and $\delta_{post} = \delta_{co}$, as appeared appropriate for small circular ruptures, postseismic to coseismic moment ratios are between 0.2 and 0.6. Such moment ratios are only slightly larger than most observations of postseismic slip in large earthquakes. It thus seems at least plausible that the difference in postseismic moments between large and small earthquakes could be reconciled by considering the geometries and durations of observations.

If geometry plays a major role in determining postseismic slip, one would expect to see a change in the postseismic to coseismic moment ratio when the earthquake geometry becomes more elongate. Seismogenic zone widths vary, but the widths of earthquakes generally start to exceed the continental seismogenic zone width as their magnitudes exceed 6 or 7. In the published literature, most $M \leq 6$ earthquakes have postseismic slip with moment larger than the coseismic moment [*Langbein et al.*, 2006; *Freed*, 2007; *Furuya and Satyabala*, 2008; *Bell et al.*, 2012; *Fattahi et al.*, 2015], while most $6 < M \leq 7$ earthquakes do not [e.g., *Donnellan and Lyzenga*, 1998; *Amoruso and Crescentini*, 2009; *Cheloni et al.*, 2010; *Johanson and Bürgmann*, 2010; *Cetin et al.*, 2012; *D'Agostino et al.*, 2012]. However, the large afterslip after $5 < M < 6$ earthquakes could be an observational bias. The afterslip of smaller earthquakes may be observable only when it is unusually large.

If geometry is not an important factor, the differences in postseismic slip between large and small earthquakes could result from changes in the frictional properties or in the mechanisms of afterslip. The deep afterslip of large earthquakes commonly occurs near the brittle-ductile transition, and the change from seismic to aseismic sliding is likely controlled by temperature. The temperature change can produce a large change in the velocity dependence of friction that may limit the afterslip moment [e.g., *Tse and Rice*, 1986; *Blanpied et al.*, 1998; *Nakatani*, 2001; *Chernak and Hirth*, 2010; *Violay et al.*, 2012]. In contrast, the seismic to aseismic transition near small earthquakes may be controlled by rheological properties or fluid pressure [*Kato*, 2008; *Chen and Lapusta*, 2009; *Niemeijer and Collettini*, 2013; *Niemeijer and Vissers*, 2014]. The frictional properties near the transition may allow for large postseismic slip.

The SAF near San Juan Bautista may be especially prone to such large afterslip. As noted above, large postseismic slip has been observed for three M 5–6 earthquakes on creeping sections of the San Andreas and Calaveras Faults: the 1998 San Juan Bautista, 2004 Parkfield, and 2007 Alum Rock earthquakes [*Langbein et al.*, 2006; *Freed*, 2007; *Barbot et al.*, 2009; *Murray-Moraleda and Simpson*, 2009; *Taira et al.*, 2014]. Small earthquakes on other faults may have smaller afterslip.

7.2. Early Evolution of Moment Rate

Afterslip moment rate is often observed to decay as t^{-1}, where t is time, so that afterslip moment accumulates logarithmically, as $\log(t)$ [e.g., *Marone et al.*, 1991; *Perfettini and Avouac*, 2004; *Savage and Langbein*, 2008; *Lin et al.*, 2013; *Hsu et al.*, 2006]. However, this scaling must change at very short timescales, or it would predict infinite slip rates at the time of the earthquake. In one modification that is consistent with velocity-strengthening frictional sliding, afterslip accumulates as $\log(t/t_c + 1)$, with a moment rate of $(t/t_c + 1)^{-1}$. Here t_c is a cutoff time, which depends on the frictional parameters and the size of the slipping region. It is the duration of an initiation period, an interval when the moment rate increases, or at least decays more slowly than t^{-1} [e.g., *Marone et al.*, 1991; *Montési*, 2004; *Perfettini and Avouac*, 2004; *Perfettini and Ampuero*, 2008]. *Montési* [2004] showed that t_c is the ratio of the slip rate in the postseismic region before the earthquake to the initial acceleration produced by the coseismic stress change. Cutoff times have been identified for a handful of earthquakes. Estimated cutoff times t_c include 3 days, after the 2005 M 8.7 Nias earthquake [*Hsu et al.*, 2006]; 1 h, after the 2003 M 8.0 Tokachi-oki earthquake [*Fukuda et al.*, 2009]; 56 days, after the 1994 M 7.6 Sanriku earthquake [*Heki et al.*, 1997]; 3 days, after the 1997 M 7.8 Kronotsky earthquake [*Bürgmann et al.*, 2001]; 20 days, after the 2010 M 7.2 El Mayor-Cucapah earthquake [*Gonzalez-Ortega et al.*, 2014], and minutes to hours [*Langbein et al.*, 2006] or 2 weeks [*Freed*, 2007], after the 2004 M 6 Parkfield earthquake. In addition, *Langbein et al.* [2006] noted that surface creep did not start in earnest until a few hours after the 2004 Parkfield earthquake, and *Dogan et al.* [2014] identified insignificant surface slip in the first 4 h after the 2011 M 7.2 Van earthquake. On the other hand, *Borcherdt et al.* [2006] did observe a rapid and large volumetric strain change—up to 70% of the coseismic strain—between 20 s and 5 min after the 2004 Parkfield earthquake. The 2014 M 6.1 South Napa earthquake showed significant shallow afterslip starting within hours of the seismic rupture [*Brocher et al.*, 2015; *Wei et al.*, 2015; *Floyd et al.*, 2016; *Lienkaemper et al.*, 2016]. For other earthquakes, most of which lack resolution on timescales of minutes to hours, no cutoff time is required to match the data. The success of a t^{-1} moment rate for these events suggests that many cutoff times are smaller than a few days, the typical minimum observation period of GPS and interferometric synthetic aperture radar data [e.g., *Marone et al.*, 1991; *Perfettini and Avouac*, 2004; *Savage and Langbein*, 2008; *Lin et al.*, 2013].

In this study, the strain data enable us to probe shorter timescales. As discussed in section 6.2, the strain rate decays more slowly than t^{-1} in the first few hours, at least for the well-resolved M 2.7–3.5 groups. The data are well fit by $\log(t/t_c + 1)$ accumulation of moment with cutoff times t_c between 0.5 and 5 h. These cutoff times are similar to the cutoff time obtained for the 2004 M 6 Parkfield earthquake by *Langbein et al.* [2006], though they are smaller than the 2 week cutoff time obtained by *Freed* [2007]. The 0.5–5 h cutoff times are also smaller than the t_c values obtained for other large earthquakes. The shorter cutoff times seen in the strain data may reflect a difference in the available observations or an actual difference in onset times for large and small earthquakes. In addition, we should note that while a deviation from a t^{-1} moment rate decay is required by the data, the cutoff time parameterization is not. There are only a few well-resolved data points in each time series, so the data could likely be matched by a form that differs from $\log(t/t_c + 1)$, such as an exponential decay (as in *Montési* [2004] and *Savage* [2007]).

An important modification of the afterslip parameterization could come from changes in the location of the slipping region with time. For instance, *Amoruso and Crescentini* [2009] observed a diffusive growth of the afterslip zone after the M 6.3 L'Aquila earthquake. *Peng and Zhao* [2009] observed a diffusion of aftershocks in the minutes to weeks following the 2004 M 6 Parkfield earthquake, and *Lengliné et al.* [2012] observed an along-strike expansion of aftershocks after Tohoku. Models of frictional slip also predict a growth of the slipping region with time [e.g., *Perfettini and Ampuero*, 2008; *Ariyoshi et al.*, 2009; *Dublanchet et al.*, 2013]. The afterslip moment rate may increase or decay more slowly than t^{-1} during this spatial growth.

The behavior of early afterslip may also provide information about its relationship with aftershocks. Aftershock rates usually follow a modified Omori decay: $(t+c)^{-p}$ where p is often close to 1 and c is a cutoff time [e.g., *Utsu et al.*, 1995]. The implied proportionality between afterslip and aftershocks has led researchers to propose that on-fault or near-fault aftershocks are triggered by postseismic slip [*Perfettini and Avouac*, 2004; *Perfettini et al.*, 2005]. Aftershock cutoff times c can be difficult to determine because earthquake catalogs are often incomplete just after earthquakes [*Kagan*, 2004]. Analysis of enhanced catalogs give aftershock cutoff times of $<$ 0.3 s, after M 0.9–3.2 repeating earthquakes near Parkfield, CA [*Lengliné and Ampuero*, 2015]; 15 min, after M 3–5 earthquakes in Japan [*Peng et al.*, 2007]; 100 s, after the 2004 M 6 Parkfield earthquake [*Peng et al.*, 2006]; 4 min, after the 2004 M 6.6 mid-Niigata earthquake [*Enescu et al.*, 2007]; less than a few minutes, after 4 M 6.6–6.7 earthquakes in Japan [*Enescu et al.*, 2009]; $<$ 40 s, after the 2008 M 6.9 Iwate-Miyagi Nairiku earthquake; and $<$ 10 min, after the 2011 *M* 9 Tohoku earthquake [*Lengliné et al.*, 2012]. The observed aftershock cutoff times thus vary among the earthquakes, but all estimates of *c* are smaller than the afterslip cutoff times estimated for the *M* 2.7–3.5 earthquakes in this study. The apparent difference in cutoff times may imply that most early aftershocks are triggered directly by the coseismic slip and that the aftershock cutoff times reflect that triggering mechanism [e.g., *Dieterich*, 1994].

7.3. Postseismic Slip Versus Poroelastic Relaxation

We have interpreted the observed postseismic strain as the result of afterslip. However, another explanation is that afterslip is small, and the observed strain results from poroelastic relaxation. In this interpretation, the coseismic strain step reflects the instantaneous deformation that occurs with little movement of pore fluid. In situ deformation of the pore fluid initially takes up some of the stress applied by the earthquake, but then the pore fluid diffuses to its equilibrium state, and the elastic rock must deform further to take up the coseismic stress [e.g., *Peltzer et al.*, 1996, 1998; *Jónsson et al.*, 2003].

In Text S11.1, we consider the plausibility of pore pressure diffusion on the 1 to 10 km scale—over distances comparable to the earthquake-strainmeter distance—as an explanation for the postseismic strain at SJT. We find that the observed strain is far larger than expected for typical crustal properties and far larger than observed for other earthquakes [*Peltzer et al.*, 1996, 1998; *Jónsson et al.*, 2003].

Earthquake-induced poroelastic deformation can sometimes be much larger in near-surface aquifers, as static and dynamic deformation can change the local permeability, connectivity, or density structure [e.g., *Quilty and Roeloffs*, 1997; *Roeloffs*, 1998; *Chia et al.*, 2001; *Matsumoto et al.*, 2003; *Wang et al.*, 2004; *Manga and Wang*, 2007]. In Text S11.2, we search for indications of strong near-surface poroelastic responses to other signals occurring near the strainmeter. First, we look for a response to ground shaking but find that the observed strain changes are better predicted as a result of static stress changes. Second, we examine the response to atmospheric pressure but obtain inconclusive results. The data permit a heterogeneous poroelastic response anywhere between zero and 100% of the applied strain. Finally, we examine the strain associated with nearby creep events [*Gladwin et al.*, 1994]. Strain in these events accumulates over 1 to 2 h. In the following 1.5 days the strain typically changes by less than 10%, suggesting that there is little to no poroelastic relaxation.

These results provide no clear evidence for significant poroelastic strain at SJT, and we conclude that afterslip is a more likely explanation. On the other hand, the data do not clearly exclude poroelastic deformation after the earthquakes. It is possible that the stress distributions induced by local earthquakes are exceptionally well oriented to produce much larger poroelastic strain than that produced by creep events or dynamic stresses.

The signs of the observed postseismic ϵ_{E-N} strains cannot distinguish between poroelastic strain and afterslip because both effects are expected to produce strain with the same sign as the coseismic strain. For ϵ_{E+N} and ϵ_{2EN}, the sign of the poroelastic strain produced by the earthquakes varies quickly in space near the strainmeter, so it is difficult to resolve (Figure S28). The similarity in the signs of afterslip and poroelastic relaxation for ϵ_{E-N} suggests that if there is significant poroelastic deformation, we are modeling it as additional afterslip and overestimating the afterslip moment. Our afterslip estimates are therefore upper bounds, and we can affirm our conclusion that the postseismic slip after small earthquakes is moderate in magnitude. Even if there is significant poroelastic strain, which we consider unlikely, the afterslip moment is of the same order as the coseismic moment, not 10 times larger as would be required to explain the recurrence intervals of small repeating earthquakes [*Nadeau and Johnson*, 1998; *Chen and Lapusta*, 2009].

7.4. Implications for Repeating Earthquake Models

As discussed in section 2, large afterslip was proposed by *Chen and Lapusta* [2009] as part of an explanation of the long recurrence intervals of repeating earthquakes [*Nadeau and Johnson*, 1998; *Nadeau et al.*, 2004; *Chen et al.*, 2007]. In their model, *Chen and Lapusta* [2009] obtained postseismic to coseismic moment ratios of up to 100 for the smallest earthquakes. Our results imply that the postseismic slip immediately following small earthquakes is not exceptionally large. This moderate afterslip may suggest that the long recurrence intervals are better explained by other hypotheses. For instance, stress drops may vary with earthquake magnitude [*Nadeau and Johnson*, 1998; *Nadeau et al.*, 2004; *Dreger et al.*, 2007], though no magnitude dependence has been seen in stress drops obtained near Parkfield, CA, where many repeating earthquakes occur [*Imanishi et al.*, 2004; *Imanishi and Ellsworth*, 2006; *Allmann and Shearer*, 2007; *Abercrombie*, 2014]. Alternatively, sections of the fault containing repeating earthquakes may be partially locked [*Anooshehpoor and Brune*, 2001;

Sammis and Rice, 2001]. Or aseismic slip could accommodate the long recurrence intervals, as long at it occurs over longer timescales than those investigated here [*Beeler et al.*, 2001; *Chen and Lapusta*, 2009].

In this study, we have examined only 1.5 days of postseismic moment because signals at longer timescales are poorly resolved by the data. If we extrapolate the short timescale signals with the assumption that moment rate decays as t^{-1} for $t > 1.5$ days, it would take at least 200 years for the postseismic moment to reach just 5 times the coseismic moment. These extrapolations suggest that the postseismic moment will not reach 10 or 100 times the coseismic moment before the next repeating earthquake, as would be expected to explain the observed recurrence intervals with moderate stress drops.

More aseismic moment can be accumulated if the postseismic moment rate stops decreasing at some point in the postseismic period. *Beeler et al.* [2001] and *Chen and Lapusta* [2009] model significant accumulation of slip throughout the interseismic period, with the moment rate increasing up to the time of the next earthquake. In the rate and state models of *Chen and Lapusta* [2009], however, the maximum interseismic moment observed on the earthquake patch was around 5 times the coseismic moment in simulations without large early afterslip. Such aseismic moment is too small to explain the long recurrence intervals of many of the small repeating earthquakes near Parkfield.

As another way to explain the long recurrence intervals and the moderate postseismic strain, one might note that most of the earthquakes considered in this study are normal earthquakes, not repeaters. One might imagine that some property of repeating earthquake patches facilitates larger postseismic slip than observed in most earthquakes. However, in section 6.3 we isolated the strain associated with some of the repeating earthquakes identified by *Templeton et al.* [2008]. The postseismic strain of these repeaters is moderate—less than twice the coseismic strain—and similar to that observed for the entire earthquake set.

8. Conclusions

We have examined the postseismic moments of small earthquakes near San Juan Bautista. Our results indicate that, on average, the postseismic moment accumulated with 1.5 days of the earthquake is 50 to 150% of the coseismic moment. This afterslip moment is larger than that typically observed following $M > 6$ earthquakes. However, within the M 1.9–5 range considered here, the ratio of postseismic to coseismic moment does not vary systematically with magnitude. The constant ratio is consistent with a simple model of earthquakes that are self-similar across a range of magnitudes. The postseismic moment is much smaller than required to explain the long recurrence intervals of small repeating earthquakes [*Nadeau and Johnson*, 1998; *Nadeau et al.*, 2004; *Chen et al.*, 2007]. The moderate observed postseismic moment may contradict the hypothesis that much of the moment associated with small repeating earthquakes accumulates as afterslip [*Chen and Lapusta*, 2009].

Acknowledgments
Strain and creep data are provided by the United States Geological Survey and are available at http://earthquake.usgs.gov/monitoring/deformation/data/download/table.php. The NCSN earthquake catalog is available at http://www.ncedc.org/ncedc/catalog-search.html, through the Northern California Earthquake Data Center and the Berkeley Seismological Laboratory, doi 10.7932/NCEDC. Earthquake relocations were taken from *Waldhauser* [2009], also available through the NCEDC. The plotted fault traces are taken from the Quaternary fault and fold database for the United States, provided by the USGS and the California Geological Survey, and accessed from the USGS website http://earthquake.usgs.gov/hazards/qfaults/. Modeled atmospheric values are from the ECMWF model, available at http://apps.ecmwf.int/datasets/ [*Dee et al.*, 2011]. Local atmospheric pressure data are from the Plate Boundary Observatory station B058, operated by UNAVCO with support from NSF, and available at http://www.unavco.org/data/strain-seismic/bsm-data/bsm-data.html. This work was supported by a Caltech Division of Geological and Planetary Sciences Texaco postdoctoral fellowship to J.C.H. We thank Nadia Lapusta for interesting discussions. We are grateful to the Associate Editor, Andy Barbour, and an anonymous reviewer for comments that improved the paper.

References

Abercrombie, R. E. (1995), Earthquake locations using single-station deep borehole recordings: Implications for microseismicity on the San Andreas fault in southern California, *J. Geophys. Res.*, *100*(B12), 24,003–24,014, doi:10.1029/95JB02396.

Abercrombie, R. E. (2014), Stress drops of repeating earthquakes on the San Andreas Fault at Parkfield, *Geophys. Res. Lett.*, *41*(24), 8784–8791, doi:10.1002/2014GL062079.

Aki, K., and P. G. Richards (2002), *Quantitative Seismology*, 2nd ed., Univ. Science Books, Sausalito, Calif.

Allmann, B. P., and P. M. Shearer (2007), Spatial and temporal stress drop variations in small earthquakes near Parkfield, California, *J. Geophys. Res.*, *112*, B04305, doi:10.1029/2006JB004395.

Amoruso, A., and L. Crescentini (2009), Slow diffusive fault slip propagation following the 6 April 2009 L'Aquila earthquake, Italy, *Geophys. Res. Lett.*, *36*, L24306, doi:10.1029/2009GL041503.

Anooshehpoor, A., and J. N. Brune (2001), Quasi-static slip-rate shielding by locked and creeping zones as an explanation for small repeating earthquakes at Parkfield, *Bull. Seismol. Soc. Am.*, *91*(2), 401–403, doi:10.1785/0120000105.

Ariyoshi, K., T. Hori, J.-P. Ampuero, Y. Kaneda, T. Matsuzawa, R. Hino, and A. Hasegawa (2009), Influence of interaction between small asperities on various types of slow earthquakes in a 3-D simulation for a subduction plate boundary, *Gondwana Res.*, *16*(3–4), 534–544, doi:10.1016/j.gr.2009.03.006.

Barbot, S., Y. Hamiel, and Y. Fialko (2008), Space geodetic investigation of the coseismic and postseismic deformation due to the 2003 M_w 7.2 Altai earthquake: Implications for the local lithospheric rheology, *J. Geophys. Res.*, *113*, B03403, doi:10.1029/2007JB005063.

Barbot, S., Y. Fialko, and Y. Bock (2009), Postseismic deformation due to the M_w 6.0 2004 Parkfield earthquake: Stress-driven creep on a fault with spatially variable rate-and-state friction parameters, *J. Geophys. Res.*, *114*, B07405, doi:10.1029/2008JB005748.

Barbour, A. J., D. C. Agnew, and F. K. Wyatt (2015), Coseismic strains on Plate Boundary Observatory borehole strainmeters in southern California, *Bull. Seismol. Soc. Am.*, *105*(1), 431–444, doi:10.1785/0120140199.

Beeler, N. M., D. L. Lockner, and S. H. Hickman (2001), A simple stick-slip and creep-slip model for repeating earthquakes and its implication for microearthquakes at Parkfield, *Bull. Seismol. Soc. Am.*, *91*(6), 1797–1804, doi:10.1785/0120000096.

Bell, J. W., F. Amelung, and C. D. Henry (2012), InSAR analysis of the 2008 Reno-Mogul earthquake swarm: Evidence for westward migration of Walker Lane style dextral faulting, *Geophys. Res. Lett.*, *39*(18), L18306, doi:10.1029/2012GL052795.

Blanpied, M. L., C. J. Marone, D. A. Lockner, J. D. Byerlee, and D. P. King (1998), Quantitative measure of the variation in fault rheology due to fluid-rock interactions, *J. Geophys. Res.*, *103*(B5), 9691–9712, doi:10.1029/98JB00162.

Borcherdt, R. D., M. J. S. Johnston, G. Glassmoyer, and C. Dietel (2006), Recordings of the 2004 Parkfield earthquake on the General Earthquake Observation System array: Implications for earthquake precursors, fault rupture, and coseismic strain changes, *Bull. Seismol. Soc. Am.*, *96*(4B), 73–89, doi:10.1785/0120050827.

Brocher, T. M. (2005), Empirical relations between elastic wavespeeds and density in the Earth's crust, *Bull. Seismol. Soc. Am.*, *95*(6), 2081–2092, doi:10.1785/0120050077.

Brocher, T. M., et al. (2015), The M_w 6.0 24 August 2014 South Napa earthquake, *Seismol. Res. Lett.*, *86*(2A), 309–326, doi:10.1785/0220150004.

Bruhat, L., S. Barbot, and J.-P. Avouac (2011), Evidence for postseismic deformation of the lower crust following the 2004 M_w6.0 Parkfield earthquake, *J. Geophys. Res.*, *116*(B8), B08401, doi:10.1029/2010JB008073.

Brune, J. N. (1970), Tectonic stress and the spectra of seismic shear waves from earthquakes, *J. Geophys. Res.*, *75*, 4997–5009, doi:10.1029/JB075i026p04997.

Bürgmann, R., M. G. Kogan, V. E. Levin, C. H. Scholz, R. W. King, and G. M. Steblov (2001), Rapid aseismic moment release following the 5 December, 1997 Kronotsky, Kamchatka, Earthquake, *Geophys. Res. Lett.*, *28*(7), 1331–1334, doi:10.1029/2000GL012350.

Cattin, R., P. Briole, H. Lyon-Caen, P. Bernard, and P. Pinettes (1999), Effects of superficial layers on coseismic displacements for a dip-slip fault and geophysical implications, *Geophys. J. Intern.*, *137*(1), 149–158, doi:10.1046/j.1365-246x.1999.00779.x.

Cetin, E., M. Meghraoui, Z. Cakir, A. M. Akoglu, O. Mimouni, and M. Chebbah (2012), Seven years of postseismic deformation following the 2003 M_w 6.8 Zemmouri earthquake (Algeria) from InSAR time series, *Geophys. Res. Lett.*, *39*(10), L10307, doi:10.1029/2012GL051344.

Cheloni, D., et al. (2010), Coseismic and initial post-seismic slip of the 2009 M_w 6.3 L'Aquila earthquake, Italy, from GPS measurements, *Geophys. J. Intern.*, *181*(3), 1539–1546, doi:10.1111/j.1365-246X.2010.04584.x.

Chen, K. H., R. M. Nadeau, and R.-J. Rau (2007), Towards a universal rule on the recurrence interval scaling of repeating earthquakes?, *Geophys. Res. Lett.*, *34*, L16308, doi:10.1029/2007GL030554.

Chen, Q., and J. T. Freymueller (2002), Geodetic evidence for a near-fault compliant zone along the San Andreas Fault in the San Francisco Bay area, *Bull. Seismol. Soc. Am.*, *92*(2), 656–671, doi:10.1785/0120010110.

Chen, T., and N. Lapusta (2009), Scaling of small repeating earthquakes explained by interaction of seismic and aseismic slip in a rate and state fault model, *J. Geophys. Res.*, *114*, B01311, doi:10.1029/2008JB005749.

Chen, X., P. M. Shearer, and R. E. Abercrombie (2012), Spatial migration of earthquakes within seismic clusters in Southern California: Evidence for fluid diffusion, *J. Geophys. Res.*, *117*(B4), B04301, doi:10.1029/2011JB008973.

Chernak, L. J., and G. Hirth (2010), Deformation of antigorite serpentinite at high temperature and pressure, *Earth Planet. Sci. Lett.*, *296*(1–2), 23–33, doi:10.1016/j.epsl.2010.04.035.

Chia, Y., Y.-S. Wang, J. J. Chiu, and C.-W. Liu (2001), Changes of groundwater level due to the 1999 Chi-Chi earthquake in the Choshui River alluvial fan in Taiwan, *Bull. Seismol. Soc. Am.*, *91*(5), 1062–1068, doi:10.1785/0120000726.

Chlieh, M., et al. (2007), Coseismic slip and afterslip of the great M_w 9.15 Sumatra–Andaman earthquake of 2004, *Bull. Seismol. Soc. Am.*, *97*(1A), 152–173, doi:10.1785/0120050631.

D'Agostino, N., D. Cheloni, G. Fornaro, R. Giuliani, and D. Reale (2012), Space-time distribution of afterslip following the 2009 L'Aquila earthquake, *J. Geophys. Res.*, *117*(B2), B02402, doi:10.1029/2011JB008523.

Dee, D. P., et al. (2011), The ERA-Interim reanalysis: configuration and performance of the data assimilation system, *Q. J. R. Meteorolog. Soc.*, *137*(656), 553–597, doi:10.1002/qj.828.

Dieterich, J. (1994), A constitutive law for rate of earthquake production and its application to earthquake clustering, *J. Geophys. Res.*, *99*(B2), 2601–2618, doi:10.1029/93JB02581.

Dogan, U., D. Ö. Demir, Z. Çakir, S. Ergintav, H. Ozener, A. M. Akoğlu, S. S. Nalbant, and R. Reilinger (2014), Postseismic deformation following the M_w 7.2, 23 October 2011 Van earthquake (Turkey): Evidence for aseismic fault reactivation, *Geophys. Res. Lett.*, *41*(7), 2334–2341, doi:10.1002/2014GL059291.

Donnellan, A., and G. A. Lyzenga (1998), GPS observations of fault afterslip and upper crustal deformation following the Northridge earthquake, *J. Geophys. Res.*, *103*(B9), 21,285–21,297, doi:10.1029/98JB01487.

Dreger, D., R. M. Nadeau, and A. Chung (2007), Repeating earthquake finite source models: Strong asperities revealed on the San Andreas Fault, *Geophys. Res. Lett.*, *34*, L23302, doi:10.1029/2007GL031353.

Dublanchet, P., P. Bernard, and P. Favreau (2013), Interactions and triggering in a 3-D rate-and-state asperity model, *J. Geophys. Res.*, *118*(5), 2225–2245, doi:10.1002/jgrb.50187.

Eberhart-Phillips, D., and A. J. Michael (1993), Three-dimensional velocity structure, seismicity, and fault structure in the Parkfield Region, central California, *J. Geophys. Res.*, *98*(B9), 15,737–15,758, doi:10.1029/93JB01029.

Enescu, B., J. Mori, and M. Miyazawa (2007), Quantifying early aftershock activity of the 2004 mid-Niigata Prefecture earthquake (M_w 6.6), *J. Geophys. Res.*, *112*(B4), B04310, doi:10.1029/2006JB004629.

Enescu, B., J. Mori, M. Miyazawa, and Y. Kano (2009), Omori-Utsu law c-values associated with recent moderate earthquakes in Japan, *Bull. Seismol. Soc. Am.*, *99*(2A), 884–891, doi:10.1785/0120080211.

Fattahi, H., F. Amelung, E. Chaussard, and S. Wdowinski (2015), Coseismic and postseismic deformation due to the 2007 M5.5 Ghazaband fault earthquake, Balochistan, Pakistan, *Geophys. Res. Lett.*, *42*(9), 3305–3312, doi:10.1002/2015GL063686.

Floyd, M. A. et al. (2016), Spatial variations in fault friction related to lithology from rupture and afterslip of the 2014 South Napa, California, earthquake, *Geophys. Res. Lett.*, *43*(13), 6808–6816, doi:10.1002/2016GL069428.

Freed, A. M. (2007), Afterslip (and only afterslip) following the 2004 Parkfield, California, earthquake, *Geophys. Res. Lett.*, *34*(6), L06312, doi:10.1029/2006GL029155.

Fukuda, J., K. M. Johnson, K. M. Larson, and S. Miyazaki (2009), Fault friction parameters inferred from the early stages of afterslip following the 2003 Tokachi-oki earthquake, *J. Geophys. Res.*, *114*, B04412, doi:10.1029/2008JB006166.

Furuya, M., and S. P. Satyabala (2008), Slow earthquake in Afghanistan detected by InSAR, *Geophys. Res. Lett.*, *35*(6), L06309, doi:10.1029/2007GL033049.

Gahalaut, V. K., et al. (2008), GPS measurements of postseismic deformation in the Andaman-Nicobar region following the giant 2004 Sumatra–Andaman earthquake, *J. Geophys. Res.*, *113*(B8), B08401, doi:10.1029/2007JB005511.

Gladwin, M. T., R. L. Gwyther, R. Hart, M. Francis, and M. J. S. Johnston (1987), Borehole tensor strain measurements in California, *J. Geophys. Res.*, *92*(B8), 7981–7988, doi:10.1029/JB092iB08p07981.

Gladwin, M. T., R. L. Gwyther, R. H. G. Hart, and K. S. Breckenbridge (1994), Measurements of the strain field associated with episodic creep events on the San Andreas fault at San Juan Bautista, California, *J. Geophys. Res.*, *99*, 4559–4565, doi:10.1029/93JB02877.

Gonzalez-Ortega, A., Y. Fialko, D. Sandwell, F. Alejandro Nava-Pichardo, J. Fletcher, J. Gonzalez-Garcia, B. Lipovsky, M. Floyd, and G. Funning (2014), El Mayor-Cucapah (M_w 7.2) earthquake: Early near-field postseismic deformation from InSAR and GPS observations, *J. Geophys. Res.*, *119*(2), 1482–1497, doi:10.1002/2013JB010193.

Hart, D. J., and H. F. Wang (1995), Laboratory measurements of a complete set of poroelastic moduli for Berea sandstone and Indiana limestone, *J. Geophys. Res.*, *100*(B9), 17,741–17,751, doi:10.1029/95JB01242.

Hart, R. H. G., M. T. Gladwin, R. L. Gwyther, D. C. Agnew, and F. K. Wyatt (1996), Tidal calibration of borehole strain meters: Removing the effects of small-scale inhomogeneity, *J. Geophys. Res.*, *101*(B11), 25,553–25,571, doi:10.1029/96JB02273.

Hawthorne, J. C., and A. M. Rubin (2013), Short-time scale correlation between slow slip and tremor in Cascadia, *J. Geophys. Res.*, *118*(3), 1316–1329, doi:10.1002/jgrb.50103.

Hawthorne, J. C., J.-P. Ampuero, and M. Simons (2016), A local recalibration of the magnitude scale near San Juan Bautista, CA, *Bull. Seismol. Soc. Am.*, in press.

He, J., and G. Peltzer (2010), Poroelastic triggering in the 9–22 January 2008 Nima-Gaize (Tibet) earthquake sequence, *Geology*, *38*(10), 907–910, doi:10.1130/G31104.1.

Heki, K., S. Miyazaki, and H. Tsuji (1997), Silent fault slip following an interplate thrust earthquake at the Japan Trench, *Nature*, *386*(6625), 595–598, doi:10.1038/386595a0.

Hodgkinson, K., J. Langbein, B. Henderson, D. Mencin, and A. Borsa (2013), Tidal calibration of Plate Boundary Observatory borehole strainmeters, *J. Geophys. Res.*, *118*(1), 447–458, doi:10.1029/2012JB009651.

Hsu, Y.-J., M. Simons, J.-P. Avouac, J. Galetzka, K. Sieh, M. Chlieh, D. Natawidjaja, L. Prawirodirdjo, and Y. Bock (2006), Frictional afterslip following the 2005 Nias–Simeulue earthquake, Sumatra, *Science*, *312*(5782), 1921–1926, doi:10.1126/science.1126960.

Imanishi, K., and W. L. Ellsworth (2006), Source scaling relationships of microearthquakes at Parkfield, CA, determined using the SAFOD pilot hole seismic array, in *Earthquakes: Radiated Energy and the Physics of Faulting, Geophys. Monogr. Ser.*, vol. 170, edited by R. E. Abercrombie et al., pp. 81–90, AGU, Washington, D. C., doi:10.1029/170GM10.

Imanishi, K., W. L. Ellsworth, and S. G. Prejean (2004), Earthquake source parameters determined by the SAFOD Pilot Hole seismic array, *Geophys. Res. Lett.*, *31*(12), L12S09, doi:10.1029/2004GL019420.

Jacobs, A., D. Sandwell, Y. Fialko, and L. Sichoix (2002), The 1999 (M_w 7.1) Hector Mine, California, earthquake: Near-field postseismic deformation from ERS interferometry, *Bull. Seismol. Soc. Am.*, *92*(4), 1433–1442, doi:10.1785/0120000908.

Johanson, I. A., and R. Bürgmann (2010), Coseismic and postseismic slip from the 2003 San Simeon earthquake and their effects on backthrust slip and the 2004 Parkfield earthquake, *J. Geophys. Res.*, *115*(B7), B07411, doi:10.1029/2009JB006599.

Johnson, K. M., R. Bürgmann, and J. T. Freymueller (2009), Coupled afterslip and viscoelastic flow following the 2002 Denali Fault, Alaska earthquake, *Geophys. J. Intern.*, *176*(3), 670–682, doi:10.1111/j.1365-246X.2008.04029.x.

Jolivet, R., R. Bürgmann, and N. Houlié (2009), Geodetic exploration of the elastic properties across and within the northern San Andreas Fault zone, *Earth Planet. Sci. Lett.*, *288*(1–2), 126–131, doi:10.1016/j.epsl.2009.09.014.

Jónsson, S. (2008), Importance of post-seismic viscous relaxation in southern Iceland, *Nat. Geosci.*, *1*(2), 136–139, doi:10.1038/ngeo105.

Jónsson, S., P. Segall, R. Pedersen, and G. Björnsson (2003), Post-earthquake ground movements correlated to pore-pressure transients, *Nature*, *424*(6945), 179–183, doi:10.1038/nature01776.

Kagan, Y. Y. (2004), Short-term properties of earthquake catalogs and models of earthquake source, *Bull. Seismol. Soc. Am.*, *94*(4), 1207–1228, doi:10.1785/012003098.

Kato, N. (2008), Numerical simulation of recurrence of asperity rupture in the Sanriku region, northeastern Japan, *J. Geophys. Res.*, *113*, B06302, doi:10.1029/2007JB005515.

Langbein, J. (2004), Noise in two-color electronic distance meter measurements revisited, *J. Geophys. Res.*, *109*, B04406, doi:10.1029/2003JB002819.

Langbein, J. (2010), Effect of error in theoretical Earth tide on calibration of borehole strainmeters, *Geophys. Res. Lett.*, *37*, L21303, doi:10.1029/2010GL044454.

Langbein, J. (2015), Borehole strainmeter measurements spanning the 2014 M_w6.0 South Napa Earthquake, California: The effect from instrument calibration, *J. Geophys. Res.*, *120*(10), 7190–7202, doi:10.1002/2015JB012278.

Langbein, J., and H. Johnson (1997), Correlated errors in geodetic time series: Implications for time-dependent deformation, *J. Geophys. Res.*, *102*(B1), 591–603, doi:10.1029/96JB02945.

Langbein, J., J. R. Murray, and H. A. Snyder (2006), Coseismic and initial postseismic deformation from the 2004 Parkfield, California, earthquake, observed by global positioning system, electronic distance meter, creepmeters, and borehole strainmeters, *Bull. Seismol. Soc. Am.*, *96*(4B), S304—S320, doi:10.1785/0120050823.

Lay, T., and T. C. Wallace (1995), *Modern Global Seismology*, Academic Press, San Diego.

Lengliné, O., and J.-P. Ampuero (2015), Insights on earthquake triggering processes from early aftershocks of repeating microearthquakes, *J. Geophys. Res.*, *120*(10), 6977–6992, doi:10.1002/2015JB012287.

Lengliné, O., B. Enescu, Z. Peng, and K. Shiomi (2012), Decay and expansion of the early aftershock activity following the 2011, M_w9.0 Tohoku earthquake, *Geophys. Res. Lett.*, *39*(18), L18309, doi:10.1029/2012GL052797.

Lienkaemper, J. J., S. B. DeLong, C. J. Domrose, and C. M. Rosa (2016), Afterslip behavior following the 2014 M 6.0 South Napa earthquake with implications for afterslip forecasting on other seismogenic faults, *Seismol. Res. Lett.*, *87*(3), 609–619, doi:10.1785/0220150262.

Lin, G., C. H. Thurber, H. Zhang, E. Hauksson, P. M. Shearer, F. Waldhauser, T. M. Brocher, and J. Hardebeck (2010), A California statewide three-dimensional seismic velocity model from both absolute and differential times, *Bull. Seismol. Soc. Am.*, *100*(1), 225–240, doi:10.1785/0120090028.

Lin, Y.-N. N., et al. (2013), Coseismic and postseismic slip associated with the 2010 Maule Earthquake, Chile: Characterizing the Arauco Peninsula barrier effect, *J. Geophys. Res.*, *118*(6), 3142–3159, doi:10.1002/jgrb.50207.

Madariaga, R. (1976), Dynamics of an expanding circular fault, *Bull. Seismol. Soc. Am.*, *66*(3), 639–666.

Mahsas, A., K. Lammali, K. Yelles, E. Calais, A. M. Freed, and P. Briole (2008), Shallow afterslip following the 2003 May 21, M_w= 6.9 Boumerdes earthquake, Algeria, *Geophys. J. Intern.*, *172*(1), 155–166, doi:10.1111/j.1365-246X.2007.03594.x.

Manga, M., and C.-Y. Wang (2007), Earthquake hydrology, in *Treatise on Geophysics, vol. 4: Earthquake Seismology*, edited by H. Kanamori and G. Schubert, pp. 6054, Elsevier, Amsterdam.

Marone, C. J., C. H. Scholtz, and R. Bilham (1991), On the mechanics of earthquake afterslip, *J. Geophys. Res.*, *96*(B5), 8441–8452, doi:10.1029/91JB00275.

Matsumoto, N., G. Kitagawa, and E. A. Roeloffs (2003), Hydrological response to earthquakes in the Haibara well, central Japan—I. Groundwater level changes revealed using state space decomposition of atmospheric pressure, rainfall and tidal responses, *Geophys. J. Intern.*, *155*(3), 885–898, doi:10.1111/j.1365-246X.2003.02103.x.

Melbourne, T. I., F. H. Webb, J. M. Stock, and C. Reigber (2002), Rapid postseismic transients in subduction zones from continuous GPS, *J. Geophys. Res.*, *107*(B10), 2241, doi:10.1029/2001JB000555.

Miura, S., Y. Suwa, A. Hasegawa, and T. Nishimura (2004), The 2003 M8.0 Tokachi-Oki earthquake — How much has the great event paid back slip debts?, *Geophys. Res. Lett.*, *31*(5), L05613, doi:10.1029/2003GL019021.

Montési, L. G. J. (2004), Controls of shear zone rheology and tectonic loading on postseismic creep, *J. Geophys. Res.*, *109*(B10), B10404, doi:10.1029/2003JB002925.

Murray-Moraleda, J. R., and R. W. Simpson (2009), Geodetically inferred coseismic and postseismic slip due to the M 5.4 31 October 2007 Alum Rock earthquake, *Bull. Seismol. Soc. Am.*, *99*(5), 2784–2800, doi:10.1785/0120090017.

Nadeau, R. M., and L. R. Johnson (1998), Seismological studies at Parkfield VI: Moment release rates and estimates of source parameters for small repeating earthquakes, *Bull. Seismol. Soc. Am.*, *88*(3), 790–814.

Nadeau, R. M., A. Michelini, R. A. Uhrhammer, D. Dolenc, and T. V. McEvilly (2004), Detailed kinematics, structure and recurrence of micro-seismicity in the SAFOD target region, *Geophys. Res. Lett.*, *31*(12), L12S08, doi:10.1029/2003GL019409.

Nakatani, M. (2001), Conceptual and physical clarification of rate and state friction: Frictional sliding as a thermally activated rheology, *J. Geophys. Res.*, *106*(B7), 13,347–13,380, doi:10.1029/2000JB900453.

Niemeijer, A. R., and C. Collettini (2013), Frictional properties of a low-angle normal fault under in situ conditions: Thermally-activated velocity weakening, *Pure Appl. Geophys.*, *171*, 1–24, doi:10.1007/s00024-013-0759-6.

Niemeijer, A. R., and R. L. M. Vissers (2014), Earthquake rupture propagation inferred from the spatial distribution of fault rock frictional properties, *Earth Planet. Sci. Lett.*, *396*, 154–164, doi:10.1016/j.epsl.2014.04.010.

Okada, Y. (1985), Surface deformation due to shear and tensile faults in a half-space, *Bull. Seismol. Soc. Am.*, *75*(4), 1135–1154.

Paul, J., A. R. Lowry, R. Bilham, S. Sen, and R. Smalley (2007), Postseismic deformation of the Andaman Islands following the 26 December, 2004 Great Sumatra-Andaman earthquake, *Geophys. Res. Lett.*, *34*, L19309, doi:10.1029/2007GL031024.

Pedersen, R., S. Jónsson, T. Árnadóttir, F. Sigmundsson, and K. L. Feigl (2003), Fault slip distribution of two June 2000 M_w6.5 earthquakes in South Iceland estimated from joint inversion of InSAR and GPS measurements, *Earth Planet. Sci. Lett.*, *213*(3–4), 487–502, doi:10.1016/S0012-821X(03)00302-9.

Peltzer, G., P. Rosen, F. Rogez, and K. Hudnut (1996), Postseismic rebound in fault step-overs caused by pore fluid flow, *Science*, *273*(5279), 1202–1204, doi:10.1126/science.273.5279.1202.

Peltzer, G., P. Rosen, F. Rogez, and K. Hudnut (1998), Poroelastic rebound along the Landers 1992 earthquake surface rupture, *J. Geophys. Res.*, *103*(B12), 30,131–30,145, doi:10.1029/98JB02302.

Peng, Z., and P. Zhao (2009), Migration of early aftershocks following the 2004 Parkfield earthquake, *Nat. Geosci.*, *2*(12), 877–881, doi:10.1038/ngeo697.

Peng, Z., J. E. Vidale, and H. Houston (2006), Anomalous early aftershock decay rate of the 2004 M_w 6.0 Parkfield, California, earthquake, *Geophys. Res. Lett.*, *33*(17), L17307, doi:10.1029/2006GL026744.

Peng, Z., J. E. Vidale, M. Ishii, and A. Helmstetter (2007), Seismicity rate immediately before and after main shock rupture from high-frequency waveforms in Japan, *J. Geophys. Res.*, *112*, B03306, doi:10.1029/2006JB004386.

Percival, D. B., and A. T. Walden (1993), Spectral Analysis for Physical Applications.

Perfettini, H., and J. P. Ampuero (2008), Dynamics of a velocity strengthening fault region: Implications for slow earthquakes and postseismic slip, *J. Geophys. Res.*, *113*, B09411, doi:10.1029/2007JB005398.

Perfettini, H., and J. P. Avouac (2004), Postseismic relaxation driven by brittle creep: A possible mechanism to reconcile geodetic measurements and the decay rate of aftershocks, application to the Chi-Chi earthquake, Taiwan, *J. Geophys. Res.*, *109*, B02304, doi:10.1029/2003JB002488.

Perfettini, H., J.-P. Avouac, and J.-C. Ruegg (2005), Geodetic displacements and aftershocks following the 2001 M_w = 8.4 Peru earthquake: Implications for the mechanics of the earthquake cycle along subduction zones, *J. Geophys. Res.*, *110*, B09404, doi:10.1029/2004JB003522.

Podgorski, J., E. H. Hearn, S. McClusky, R. Reilinger, T. Taymaz, O. Tan, M. Prilepin, T. Guseva, and M. Nadariya (2007), Postseismic deformation following the 1991 Racha, Georgia, earthquake, *Geophys. Res. Lett.*, *34*(4), L04310, doi:10.1029/2006GL028477.

Pollitz, F. F., P. Banerjee, R. Burgmann, M. Hashimoto, and N. Choosakul (2006), Stress changes along the Sunda trench following the 26 December 2004 Sumatra-Andaman and 28 March 2005 Nias earthquakes, *Geophys. Res. Lett.*, *33*(6), L06309, doi:10.1029/2005GL024558.

Prieto, G. A., P. M. Shearer, F. L. Vernon, and D. Kilb (2004), Earthquake source scaling and self-similarity estimation from stacking P and S spectra, *J. Geophys. Res.*, *109*(B8), B08310, doi:10.1029/2004JB003084.

Pritchard, M. E., and M. Simons (2006), An aseismic slip pulse in northern Chile and along-strike variations in seismogenic behavior, *J. Geophys. Res.*, *111*, B08405, doi:10.1029/2006JB004258.

Quilty, E. G., and E. A. Roeloffs (1997), Water-level changes in response to the 20 December 1994 earthquake near Parkfield, California, *Bull. Seismol. Soc. Am.*, *87*(2), 310–317.

Rice, J. R., and M. P. Cleary (1976), Some basic stress diffusion solutions for fluid-saturated elastic porous media with compressible constituents, *Rev. Geophys.*, *14*(2), 227–241, doi:10.1029/RG014i002p00227.

Roeloffs, E. (2010), Tidal calibration of Plate Boundary Observatory borehole strainmeters: Roles of vertical and shear coupling, *J. Geophys. Res.*, *115*, B06405, doi:10.1029/2009JB006407.

Roeloffs, E. A. (1998), Persistent water level changes in a well near Parkfield, California, due to local and distant earthquakes, *J. Geophys. Res.*, *103*(B1), 869–889, doi:10.1029/97JB02335.

Ryder, I., B. Parsons, T. J. Wright, and G. J. Funning (2007), Post-seismic motion following the 1997 Manyi (Tibet) earthquake: InSAR observations and modelling, *Geophys. J. Intern.*, *169*(3), 1009–1027, doi:10.1111/j.1365-246X.2006.03312.x.

Ryder, I., R. Bürgmann, and J. Sun (2010), Tandem afterslip on connected fault planes following the 2008 Nima-Gaize (Tibet) earthquake, *J. Geophys. Res.*, *115*(B3), B03404, doi:10.1029/2009JB006423.

Sammis, C. G., and J. R. Rice (2001), Repeating earthquakes as low-stress-drop events at a border between locked and creeping fault patches, *Bull. Seismol. Soc. Am.*, *91*(3), 532–537, doi:10.1785/0120000075.

Savage, J. C. (2007), Postseismic relaxation associated with transient creep rheology, *J. Geophys. Res.*, *112*, B05412, doi:10.1029/2006JB004688.

Savage, J. C., and J. Langbein (2008), Postearthquake relaxation after the 2004 M6 Parkfield, California earthquake and rate-and-state friction, *J. Geophys. Res.*, *113*, B10407, doi:10.1029/2008JB005723.

Savage, J. C., and J. L. Svarc (1997), Postseismic deformation associated with the 1992 M_w 7.3 Landers earthquake, southern California, *J. Geophys. Res.*, *102*(B4), 7565–7577, doi:10.1029/97JB00210.

Schmalzle, G., T. Dixon, R. Malservisi, and R. Govers (2006), Strain accumulation across the Carrizo segment of the San Andreas Fault, California: Impact of laterally varying crustal properties, *J. Geophys. Res.*, *111*(B5), B05403, doi:10.1029/2005JB003843.

Schulz, S. S. (1989), Catalog of creepmeter measurements in California from 1966 through 1988, *Tech. Rep. 89-650*, USGS, version 1.1.

Segall, P. (2010), *Earthquake and Volcano Deformation*, Princeton Univ. Press, Princeton, N. J.

Segall, P., R. Bürgmann, and M. Matthews (2000), Time-dependent triggered afterslip following the 1989 Loma Prieta earthquake, *J. Geophys. Res.*, *105*(B3), 5615–5634, doi:10.1029/1999JB900352.

Subarya, C., M. Chlieh, L. Prawirodirdjo, J. P. Avouac, Y. Bock, K. Sieh, A. J. Meltzner, D. H. Natawidjaja, and R. McCaffrey (2006), Plate-boundary deformation associated with the great Sumatra-Andaman earthquake, *Nature*, *440*(7080), 46–51, doi:10.1038/nature04522.

Taira, T., R. Bürgmann, R. M. Nadeau, and D. S. Dreger (2014), Variability of fault slip behavior along the San Andreas Fault in the San Juan Bautista Region, *J. Geophys. Res.*, *119*(12), 8827–8844, doi:10.1002/2014JB011427.

Talwani, P., L. Chen, and K. Gahalaut (2007), Seismogenic permeability, k_s, *J. Geophys. Res.*, *112*(B7), B07309, doi:10.1029/2006JB004665.

Templeton, D. C., R. M. Nadeau, and R. Bürgmann (2008), Behavior of repeating earthquake sequences in central California and the implications for subsurface fault creep, *Bull. Seismol. Soc. Am.*, *98*(1), 52–65, doi:10.1785/0120070026.

Thurber, C., H. Zhang, F. Waldhauser, J. Hardebeck, A. Michael, and D. Eberhart-Phillips (2006), Three-dimensional compressional wavespeed model, earthquake relocations, and focal mechanisms for the Parkfield, California, region, *Bull. Seismol. Soc. Am.*, *96*(4B), 38–49, doi:10.1785/0120050825.

Tse, S. T., and J. R. Rice (1986), Crustal earthquake instability in relation to the depth variation of frictional slip properties, *J. Geophys. Res.*, *91*, 9452–9472, doi:10.1029/JB091iB09p09452.

Utsu, T., Y. Ogata, and R. S. Matsu'ura (1995), The centenary of the Omori formula for a decay law of aftershock activity, *Earth, Planet. Space*, *43*(1), 1–33, doi:10.4294/jpe1952.43.1.

Violay, M., B. Gibert, D. Mainprice, B. Evans, J.-M. Dautria, P. Azais, and P. Pezard (2012), An experimental study of the brittle-ductile transition of basalt at oceanic crust pressure and temperature conditions, *J. Geophys. Res.*, *117*(B3), B03213, doi:10.1029/2011JB008884.

Waldhauser, F. (2009), Near-real-time double-difference event location using long-term seismic archives, with application to Northern California, *Bull. Seismol. Soc. Am.*, *99*(5), 2736–2748, doi:10.1785/0120080294.

Waldhauser, F., and D. P. Schaff (2008), Large-scale relocation of two decades of Northern California seismicity using cross-correlation and double-difference methods, *J. Geophys. Res.*, *113*(B8), B08311, doi:10.1029/2007JB005479.

Wang, C.-y., C.-H. Wang, and M. Manga (2004), Coseismic release of water from mountains: Evidence from the 1999 ($M_w = 7.5$) Chi-Chi, Taiwan, earthquake, *Geology*, *32*(9), 769–772, doi:10.1130/G20753.1.

Wei, S., S. Barbot, R. Graves, J. J. Lienkaemper, T. Wang, K. Hudnut, Y. Fu, and D. Helmberger (2015), The 2014 M_w 6.1 South Napa Earthquake: A unilateral rupture with shallow asperity and rapid afterslip, *Seismol. Res. Lett.*, *86*(2A), 344–354, doi:10.1785/0220140249.

Wen, Y., Z. Li, C. Xu, I. Ryder, and R. Bürgmann (2012), Postseismic motion after the 2001 M_w 7.8 Kokoxili earthquake in Tibet observed by InSAR time series, *J. Geophys. Res.*, *117*(B8), B08405, doi:10.1029/2011JB009043.

Ziv, A. (2006), Does aftershock duration scale with mainshock size?, *Geophys. Res. Lett.*, *33*(17), L17317, doi:10.1029/2006GL027141.